Fall 2018

OPTICAL PROPERTIES OF LABORATORY GENERATED AEROSOL: COMPLEX REFRACTIVE INDEX RETRIEVAL FOR POLYSTYRENE LATEX SPHERES, AND EXTINCTION ENHANCEMENT OF MONTMORILLONITE BY WATER SWELLING

Tyler Galpin
University of New Hampshire, Durham

OPTICAL PROPERTIES OF LABORATORY GENERATED AEROSOL: COMPLEX REFRACTIVE INDEX RETRIEVAL FOR POLYSTYRENE LATEX SPHERES, AND EXTINCTION ENHANCEMENT OF MONTMORILLONITE BY WATER SWELLING

BY

TYLER R. GALPIN
Bachelor of Science, Rochester Institute of Technology, 2011

THESIS

Submitted to the University of New Hampshire

in Partial Fulfillment of

the Requirements for the Degree of

Master of Science

in

Chemistry

September, 2018

This Thesis has been examined and approved in partial fulfillment of the requirements for the degree of Master of Science in Chemistry by:

Thesis Advisor, Dr. Margaret E. Greenslade
Associate Professor, Department of Chemistry

Dr. Gonghu Li
Associate Professor, Department of Chemistry

Dr. John Tsavalas
Associate Professor, Department of Chemistry

Dr. Jack E. Dibb
Research Associate Professor, Institute for the Study of Earth, Oceans, and Space

On July 31, 2017

Approval signatures are on file with the University of New Hampshire Graduate School.

DEDICATION

This thesis is dedicated to my parents, Ken and Diane Cobb, and my brother, Brad Galpin, who have always pushed and encouraged me to reach for my goals. I consider the achievements of this manuscript to be for all of us, and I wouldn't be the man I am today without all of you.

ACKNOWLEDGEMENTS

Funding for this work was provided by the University of New Hampshire, College of Engineering and Physical Sciences, Teaching Assistantship support by the Graduate School, and the Directed Energy Professional Society scholarship fund. Instruments used for the work were purchased with the College of Engineering and Physical Sciences Dean's start up grant.

I first want to thank the members of my PhD committee Dr. Gonghu Li, Dr. John Tsavalas, Dr. Carolyn Jordan, and Dr. Jack Dibb for supplying valuable feedback in the completion of this thesis. I would also like to thank the faculty of the Chemistry Department, especially Dr. Howard Mayne, for the outstanding mentorship and learning environment created here at the university. Additionally, I would like to thank all past and present members of the Greenslade group, the "big" group, and other chemistry students for all of the thoughtful and interesting conversations.

I finally want to thank my research advisor, Dr. Margaret Greenslade, for all she has done to make me a better chemist today. Your guidance through learning about aerosol research, writing my first peer reviewed manuscript, teaching physical chemistry, and many other things is invaluable to me.

TABLE OF CONTENTS

LIST OF TABLES

LIST OF FIGURES

ABSTRACT

OPTICAL PROPERTIES OF LABORATORY GENERATED AEROSOL: COMPLEX REFRACTIVE INDEX RETRIEVAL FOR POLYSTYRENE LATEX SPHERES, AND EXTINCTION ENHANCEMENT OF MONTMORILLONITE BY WATER SWELLING

by

Tyler R. Galpin

University of New Hampshire

Aerosol can alter climate through the interaction with solar radiation by absorbing and scattering solar radiation. Absorption and scattering are governed by complex refractive index (CRI) dependent on the chemical composition and wavelength, the physical properties of the aerosol such as size, and other atmospheric parameters such as relative humidity (RH). CRI is commonly reported as the real portion at a single wavelength, or is unknown, which introduces uncertainty when those values are used as input for climate models. Two optical interrogation techniques, Aerosol Extinction Differential Absorption Spectroscopy (AE-DOAS) and Cavity Ring-Down Spectroscopy (CRD), allow for controlled measurements of laboratory generated aerosol.

The AE-DOAS has facilitated the retrieval of wavelength dependent CRI for polystyrene latex spheres (PSL). The instrument includes a white-type multi-pass gas cell coupled to a spectrometer designed to maximize sensitivity over the spectral range of 235-700 nm where

particularly the UV region is not possible with most other aerosol instruments. Retrievals are achieved by iteratively minimizing the disagreement between Mie theory and measured extinction as a function of sphere size. The PSL retrieved values show agreement to previously published literature results while expanding the range of known values.

The CRD has allowed for precise measurement of extinction for montmorillonite aerosol. The instrument includes a laser source at 532 nm and two cavities allowing for a direct comparison of measured extinction at different RH. Montmorillonite is an alumina silicate clay composed of a layered structure allowing for generated aerosol particles to swell in the presence of increased RH. Studies were conducted comparing two different generation methods, wet and dry, for aerosol samples. Experimental results indicate that the difficulty of fully drying wet generated aerosol may significantly impact the measured amount of adsorbed water.

CHAPTER 1

INTRODUCTION TO AEROSOL CHEMISTRY

1.1 CLIMATE CHANGE

Human impacts on the Earth's climate, especially increasing atmospheric concentrations of greenhouse gases, have continued since the rapid industrialization period of the 20th century (IPCC 2013). These impacts can be divided into two major parts, climate forcings and climate responses (Seinfeld and Pandis 2006). Climate forcings change the energy balance of Earth and include greenhouse gases, aerosols, and variability in the Sun's output. A compilation of the anthropogenic radiative forcing (RF, W/m^2) for the main gas (upper three chemicals) and aerosol (remaining six components, including how aerosols influence clouds) climate forcers is shown in Figure 1.1. The x-axis represents RF, a measure of the difference in energy flow for the Earth with and without the component present (IPCC 2013). Carbon dioxide (CO_2), the most prevalent greenhouse gas with anthropogenic contributions, has an RF of +1.68(18) W/m^2 for the cumulative emissions from 1750-2011, representing a component that warms the atmosphere (IPCC 2013). Organic carbon aerosols have a negative estimated RF value of -0.3(2) W/m^2 representing a component that cools (IPCC 2013). Further, the major greenhouse gases like CO_2 and CH_4 have long lifetimes in the atmosphere and are well mixed allowing for the RF of these gases to be known with a high level of confidence resulting in small relative error to the

magnitude of the values as compared to the aerosol components shown. The error bars for some aerosol, like mineral dust, span the range from negative to positive RF which indicates uncertainty in whether these components warm or cool the atmosphere.

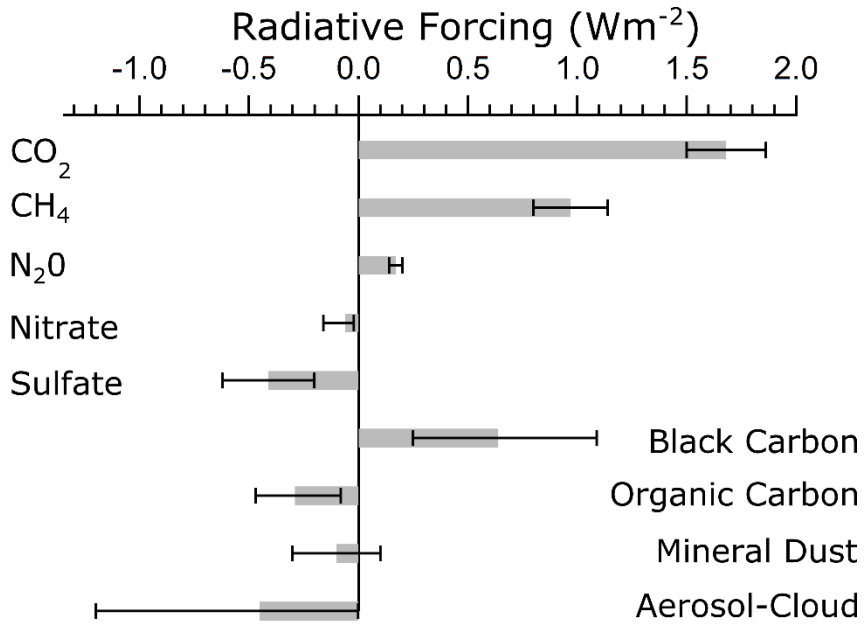

Figure 1.1. Radiative forcing from 1750-2011 for select atmospheric gas and aerosol components. The grey shaded bar represents the estimated value of RF for a particular component based off a combination of measured anthropogenic emissions and complex simulations and the black error bars show the 5 and 95 % confidence intervals. This figure is adapted from Figure TS.7 in the Technical Summary of the Intergovernmental Panel on Climate Change fifth assessment (IPCC 2013).

Warming, or cooling, for an aerosol is dependent on the amount of scattered or absorbed light. Sulfate aerosol for example absorb almost no light and only scatter as shown by an RF of -0.4(2) W/m^2 (Toon et al. 1976, IPCC 2013). Whether an aerosol component warms or cools can also be quantified with the single scattering albedo (SSA) which is a ratio of scattered light to the sum of scattered and absorbed light. The critical value of SSA = 0.85 has been shown to be a dividing line between aerosol components that warm or cool (Hansen et al. 1980). Most aerosol

have an SSA > 0.85 corresponding to the negative RF values shown in Figure 1.1. The critical value of SSA is further complicated by the underlying Earth surface below an aerosol. High albedo surfaces, like snow pack, will have a higher critical SSA because of the importance of reflected sunlight from those surfaces (Hsu et al. 2004).

Climate responses to climate forcings can be seen in many Earth systems including temperature increase, sea rise, glacier melt, increased drought occurrence, and extreme weather (Hansen et al. 2010, Church and White 2011, Lin et al. 2016). Further, climate responses and climate forcings have been shown to have adverse effects on human health and welfare (Kulp and Strauss 2017, Miller et al. 2017, Tong et al. 2017).

An aerosol is a collection of solid or liquid particles suspended in a gas. A large fraction of total aerosol atmospheric loading is produced from natural sources with the majority from sea salt and mineral dust as shown by Table 1.1 (Seinfeld and Pandis 2006). While anthropogenically produced aerosol loading is low, human actions such as changes to land use and deforestation can alter emission rates of some aerosol typically considered natural, such as mineral dust (Prospero and Lamb 2003). Aerosol effects on RF are further broken down into two subcategories, direct and indirect effects. The direct effect is defined as scattering and absorption of light (Angstrom 1929). Scattering and absorption depend on the chemical and physical properties of the particles including size, shape, complex refractive index (CRI), concentration, and spatial distribution as well as how these properties vary as a function of other atmospheric variables like relative humidity (Bohren and Huffman 1983). The indirect effect of aerosol describes how particles alter the formation and persistence of clouds thus changing global cloud

albedo (Twomey et al. 1984). A pristine clean atmosphere with only homogeneous condensation would contain almost no clouds and upon the introduction of particles a dramatic increase in cloud cover (Koren et al. 2014). Generally the largest uncertainties associated with current climate models have to do with cloud lifetimes, coverage, radiative forcing, and created precipitation as depicted by the large error bar of aerosol-cloud RF in Figure 1.1 (Twomey et al. 1984, IPCC 2013).

Table 1.1. Annual total emission for select aerosol components where the SI prefix tera is 10^{12} g which is equivalent to the mass of three Empire State Buildings. This table is adapted from Table 2.20 in Atmospheric Chemistry and Physics containing additional references therein (Seinfeld and Pandis 2006).

	Source	Estimated Global Flux (Tg/yr)
Natural	Mineral Dust	2980
	Seasalt	10100
	Volcanic Dust	30
	Biological Debris	50
	Sulfates	32.4
	Volatile Organic Compounds	11.2
Anthropogenic	Industrial Dust	100
	Black Carbon	12
	Organic Aerosol	81
	Sulfates	48.6
	Nitrates	21.3

Aerosol particles are typically found in the size range with physical diameters (d) from a few nanometers to tens of micrometers and are composed of a cluster of molecules. A range covering this many orders of magnitude is subdivided into smaller, more specific, groups such as nucleation mode, Aitken mode, accumulation mode, and coarse mode (Seinfeld and Pandis 2006). The nucleation mode contains the smallest particles with $d < 10$ nm. Nucleation mode particles are formed in the atmosphere by gas-to-particle reactions. For example, sulfates and nitrates are formed from the precursor gases SO_x and NO_x by oxidation reactions with other

gases such as hydroxyl and water, respectively (Saltzman et al. 1983, Ammann et al. 2013). Nucleated particles are small enough that gravitational settling is insignificant making the predominant removal mechanism condensation onto larger particles demonstrating a process of atmospheric ageing (Kulmala et al. 2001). The next largest mode, Aitken, is comprised of particles from 10-100 nm with formation primarily from nucleation mode particles continuing to grow. Aitken mode and nucleation mode particles make up a majority of the number of ambient particles. However, due to their small size these modes make up only a small fraction of total aerosol mass and volume. Aitken mode particles continue to grow from gas-to-particle reactions into the accumulation mode. Aitken mode particles are still too small to be efficiently removed from the atmosphere by gravitational settling as shown by Aalto et al. (2001).

Accumulation mode particles range from 100-1000 nm consisting of grown particles from smaller modes as well as directly emitted particles as shown by Krejci et al. (2005). Accumulation mode particles fall in the size range where they are large enough to account for a large fraction of aerosol surface area (47 %) yet small enough to persist in the atmosphere without settling for times on the order of weeks. With long atmospheric lifetimes long range transportation occurs which allows for atmospheric processing to change the physical and optical properties of the particles as demonstrated by Matsui et al. (2011). Ultimately, accumulation mode aerosol is removed from the atmosphere primarily by wet deposition, where particles are scavenged by water droplets falling to the surface as for example work by Krejci et al. (2005). Coarse mode contains the largest particles with $d > 1.0$ μm. Generation occurs from mechanical processes such as wind blowing over the ocean surface producing sea salt aerosol. Coarse mode particles make up the majority of total aerosol volume. However, coarse mode particles are large

enough to efficiently undergo gravitational settling with atmospheric lifetimes on the order of a day.

In addition to differences in size, aerosol particles have a range of possible morphologies (DeCarlo et al. 2004, Seinfeld and Pandis 2006). Aerosol are commonly assumed to be spherical homogenous spheres. Ammonium sulfate (AS) is a common component that forms spherical aerosol (Dick et al. 1998). Transmission electron microscopy (TEM) images of individual AS particles reveal round shapes with surface irregularities (Dick et al. 1998). For NaCl particles, TEM measurements have revealed crystalline cubic structures (Hirst and Kaye 1996, Dick et al. 1998). Both AS and NaCl particles exhibit significant water activity during atmospheric transport allowing for dynamic shape effects where particles become more spherical at elevated humidity (Dick et al. 1998).

Carbonaceous aerosol particles have been revealed to have a range of morphologies including spherical for secondary organic aerosol (SOA) (Virtanen et al. 2010). SOA can be formed in the atmosphere by gas-to-particle reactions first forming liquid clusters before transitioning to an amorphous solid state (Virtanen et al. 2010, Adler et al. 2013). SOA particles can contain internal voids (Adler et al. 2013). Research has shown that void size, shape, and occurrence can be further altered by atmospheric processing resulting in changes to particle density (Adler et al. 2013). Carbonaceous aerosol can have further non-spherical morphologies such as the fractal shape of particles composed of black carbon (Andreae and Gelencser 2006, Petzold et al. 2013).

Due to the number of different possible morphologies, there are many ways to characterize a particle's dimensions. The simplest particle to consider is spherical and composed of a single component. For this particle, the diameter (d) and other properties such as volume can be determined with basic geometry. The diameter is more difficult to define for particles that are non-spherical or contain voids. One way to describe this particle is to quantify the amount of material present using the volume equivalent diameter and mass. The volume equivalent diameter (d_{ve}) for a particle is defined as the diameter of a solid, smooth sphere with the same volume of material (DeCarlo et al. 2004). For a solid spherical particle, $d = d_{ve}$, but for a spherical particle with internal voids $d > d_{ve}$.

Other diameter definitions for a particle depend on the measurement technique (Kelly and McMurry 1992, Alexander et al. 2016). For example, one commonly used technique for aerosol size distribution characterization is the scanning mobility particle sizer (SMPS) which defines the diameter by electrical mobility (D_m). In this case D_m is defined by a sphere which migrates with the same velocity in a constant electric field as the studied particle (Fissan et al. 1983, DeCarlo et al. 2004). For a solid spherical particle $d = D_m$. For the same particle volume, as the shape becomes less spherical D_m increases since the drag on a non-spherical particle is increased compared to a sphere (Fissan et al. 1983). Another way to separate particles is with settling velocity such as with an aerosol mass spectrometer (AMS) (Jayne et al. 2000, DeCarlo et al. 2004). In this case, the aerodynamic diameter (d_a) is defined by a sphere which falls at the same terminal velocity as the studied particle. Much like with D_m, non-spherical particles have added drag resulting in increased d_a.

1.2 INTERACTION OF LIGHT WITH AEROSOL

Light scattering is depicted in Figure 1.2 by a particle of arbitrary size and shape composed of small subregions. When light is incident on the particle a momentary dipole is induced on each subregion, which oscillates emitting secondary radiation (scattered wavelet) in all angles, θ, with the same energy as the incident beam (Kerker 1969). At some distant point (P) from the particle, total scattered light is calculated by superposing the scattered wavelets from each dipole taking into account the phase of each (Bohren and Huffman 1983). In practice a measurement at P is the total amount of energy which is a function of the incident wave and scattered wavelets. In order to separate contributions from the incident and scattered waves it is necessary to view the light falling on a lens shaped area located at P. As θ becomes smaller either the lens must be increased in area or P must be moved further away suggesting that instruments with the longest path lengths will be most sensitive (van de Hulst 1981). For a particle much smaller than the wavelength of light phase variation with scattering angle is negligible meaning that scattering intensity is not a function of θ. As size increases more possibilities exist for each scattered wavelet to possess a different phase creating a scattering pattern with many minima and maxima from wave interference. In addition to geometrical considerations for scattering pattern, the amplitude and phase of each wavelet will depend on the ability of the incident light to induce a dipole on the particle subregion which is related to the permittivity and ultimately the CRI of the material, or aerosol component (Bohren and Huffman 1983). For a collection of particles it would reason that the measured scattering at P is the summation of the cooperative effect of each particle. This only holds true for the special case known as independent scattering in which each particle is separated by at least three times the average radius of the particles ensuring each

particle is illuminated by the complete power of the incident wave and allowed sufficient space to create its own scattering pattern, while the scattered radiation has no interaction with adjacent particles (Kerker 1969, van de Hulst 1981).

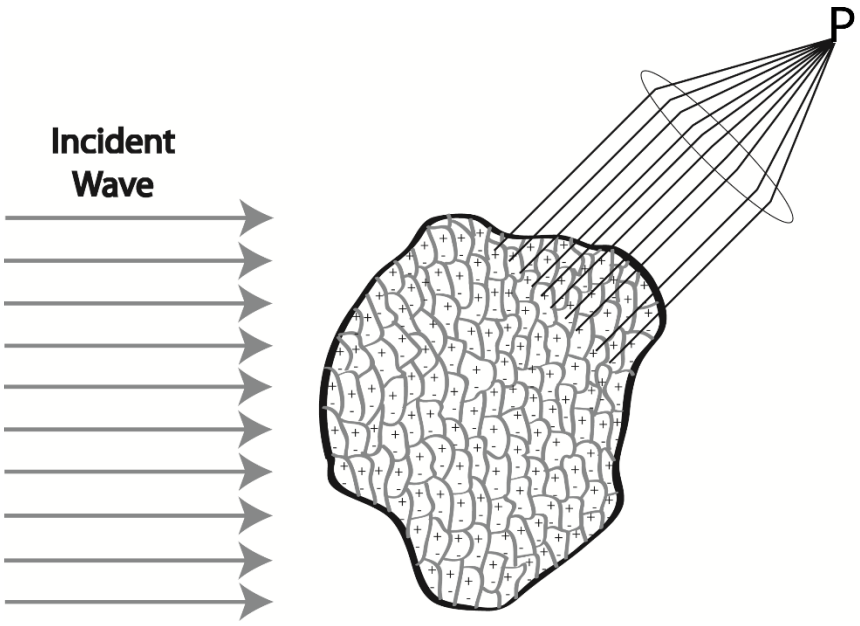

Figure 1.2. Incident wave of light on a particle of arbitrary size and shape. The particle is broken into smaller subregions each containing a dipole. The point P is assumed to be distant enough that all scattered light appears coherent. This figure is adapted from Figure 1.4 in Absorption and Scattering of Light by Small Particles (Bohren and Huffman 1983).

Absorption of light by a particle is analogous to molecular excitation. At ambient conditions electrons predominantly exist in their lowest energy level, the ground state. By stimulating electrons with an external energy input, in this case the incident wave, they will undergo a transition to a higher energy level, an excited state. After a short period of time the electrons will return to the ground state emitting excess energy, usually in the form of heat (Skoog et al. 2007). Some spectroscopists measure the emitted energy to gain insight on molecular properties but more commonly, in simple absorption spectroscopy, the amount of absorbed light (A) is measured and related to concentration (c) using the Beer-Lambert Law shown in Equation (1.1)

where ε is the molar absorptivity, and l is the path length. Various excited energy levels can be achieved including electronic, vibrational, and rotational where the energy difference between the excited and ground state is proportional to a specific wavelength of light. For most aerosol components light absorption predominantly takes place in UV and IR regions of the spectrum from electronic and vibrational excitation respectively (Bohren and Huffman 1983). Some carbon containing aerosol absorbs visible wavelengths especially particles composed of black carbon explaining the large positive RF associated with this component in Figure 1.1.

$$A = \varepsilon l c \tag{1.1}$$

The sum of scattering and absorption is extinction, or attenuation, of the incident wave. Scattering, absorption, and extinction coefficients for an aerosol are measured in units of length^{-1} describing the total amount of light lost per unit distance between source and detector. Extinction coefficients are represented by σ with a subscript to denote the interaction type, although there is some debate about this in the literature due to the similarity with notation for molecular cross sections. Most commonly Mm^{-1} and cm^{-1} are the units found in the literature. A measure that may be more familiar to chemists is the cross section measured in units of length^2 which describes light interactions for a single particle. Cross sections are typically represented by *C*, again with a subscript to denote scattering, absorption, or extinction. To remain consistent with gas phase spectroscopy and other aerosol literature the units of cm^2 are used in this work. Integrating cross section over a size distribution of particles calculates the coefficient for the whole sample.

For a particle, extinction cross section is a function of shape, size, wavelength of incident light, and CRI. These variables are used as Mie Theory inputs to calculate extinction. Mie Theory can be used when the size of the particle is comparable to the wavelength of light, however the major assumption that particles are spheres does not hold true for all aerosols especially mineral dust. Other theories exist that compute extinction for other particle shapes including roughened spheres, spheroids, and rods though the agreement with measurements can still be improved (Bohren and Huffman 1983, Hudson et al. 2008, Veghte et al. 2015).

The CRI ($m(\lambda) = n(\lambda) \pm ik(\lambda)$) is often times unknown as an input variable for Mie Theory. In the CRI equation n is the real portion of the refractive index, k is the imaginary portion, and *i* is $\sqrt{-1}$. Both n and k are wavelength dependent as denoted with λ. CRI is a physical property of an aerosol component. The real portion is defined as the ratio of the speed of light in vacuum to the speed of light in the material. As described by Snell's Law, when light enters a material it is bent, or refracted, by some angle. One way to measure n leveraging the bending of light is using an Abbe refractometer to measure the refraction for liquids at $\lambda = 589$ nm, the sodium D-line, by sandwiching the sample between two prisms of known refractive index (Dodd 1931). Most refractometers lack the ability to measure the wavelength dependence of n as they operate at a single wavelength. For aerosol particles n informs the amount of light scattered by the particle. Many instruments exist to measure light scattered by particles including nephelometers, optical particle counters, and even electrodynamic balance coupled with Mie resonance spectroscopy measurements for single particles (Charlson et al. 1974, Steimer et al. 2015). These instruments operate over a wider range of wavelengths but still fail to cover the entire solar spectrum. In reference books like the Chemical Rubber Company (CRC) Handbook of Chemistry and Physics

and Lange's Handbook of Chemistry n_D, where the subscript D denotes the sodium D-line, is listed for some aerosol components but missing for many others (Speight 2005, Haynes 2016). Data that does exist for multiple wavelengths exists because of specific targeted laboratory studies (Han et al. 2009). Several formulae exist for calculating n over a small wavelength range, like the Cauchy Dispersion relationship, the Sellmeier formula, or the Lorentz-Lorenz equation, however these have little physical meaning since they are empirically derived.

The imaginary portion of the CRI is related to the absorption of a material. Many instruments measure absorption of bulk materials including UV-Vis and FT-IR spectrometers. Typically for these instruments samples are either solids or liquids. UV-Vis allows for accurate determination of physical properties like molar absorptivity, however, absorption may not be the same between bulk and nanoscale particles because of surface mode excitation (Bohren and Huffman 1983). Some approaches exist to calculate k from the measured bulk absorption, though particularly at UV wavelengths it may be difficult to find suitable solvents which do not interfere with measured spectra (Sun et al. 2007, Chen and Bond 2010). Instruments have also been developed for the measurement of aerosol absorption including photoacoustic spectroscopy (PAS), aethalometry, particle soot absorption photometers, and multi-filter rotating shadowband radiometers (Horvath 1993, Moosmuller et al. 2009). Several of these instruments may have added uncertainty on measured absorption since they rely on depositing samples on filters which can introduce artifacts. PAS is the most promising technique for measuring absorption but is currently limited by the number of operating wavelengths especially in the UV region (Wiegand et al. 2014, Radney et al. 2017). Ultimately measuring absorption for aerosol particles can be

quite challenging because small C_{abs} values for many types of aerosol require instruments with low limits of detection.

A final series of instruments can measure extinction such as ellipsometry for bulk analysis and transmissometers, sun photometers, and cavity based spectrometers for particle measurements. A few of these instruments, including ellipsometers and broadband cavity enhanced spectroscopy operate over wide wavelength ranges into the UV where absorption becomes significant for some aerosol components (Humlicek 2005, French et al. 2007, Washenfelder et al. 2013). Ellipsometry measures the change in polarization of light reflected off a thin film of material. Much like other bulk measurements there may be discrepancies recreating the density and surface properties of particles which could yield different CRI results. The extinction results from aerosol instruments can be coupled with an iterative minimization routine to generate best fit CRI (Bluvshtein et al. 2012, Washenfelder et al. 2013, Zarzana et al. 2014). In some cases the retrieved values compare favorably to other literature results (Spindler et al. 2007, Dinar et al. 2008). However, retrieving CRI from extinction can be challenging since it is difficult to separate scattering and absorption (Bohren and Huffman 1983). The error on retrieved CRI can be improved by measuring multiple particle sizes where scattering and absorption respond differently to changes in diameter as shown by Figure 1.3 (Bluvshtein et al. 2012, Zarzana et al. 2014). For the two combinations of n and k, Mie Theory calculations of % of total extinction, for either scattering or absorption, show different relationships as a function of diameter. Others have paired extinction measurements with either a complimentary scattering or absorption measurement (Gerber 1979, Arnott et al. 1999, Lack et al. 2006). Calculating absorption from a subtraction method can be particularly challenging because extinction is predominated by

scattering as demonstrated by most aerosol components having SSA > 0.85 (Hansen et al. 1980, Singh et al. 2014).

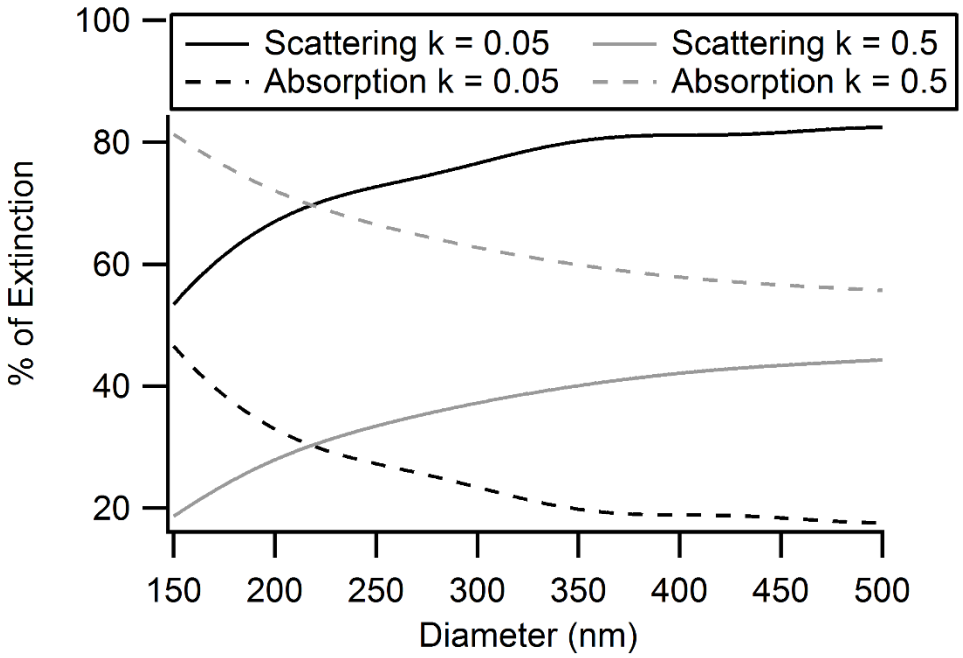

Figure 1.3. Mie Theory calculations of % of total extinction for scattering and absorption as a function of particle diameter. In all cases n = 1.50. The black solid line and dashed line represent k = 0.05 for scattering and absorption, respectively and the grey solid line and dashed line represent k = 0.5 for scattering and absorption, respectively.

Particle morphology will also have an effect in determining the CRI for a particle. For a solid, spherical, single component particle the CRI is equivalent to the bulk material. Many ambient aerosol particles are multicomponent or contain internal voids resulting in challenges in determining the CRI. For a particle with internal voids the CRI is lower than a solid particle with the same dimensions since the light must pass through some amount of air within. Mathematically representing the contribution of the voids to CRI is challenging and further, is complicated by a lack of knowledge about the location and size of voids for *in situ* particles.

1.3 AMBIENT AEROSOL MEASUREMENTS

Significant interest exists in measuring spatial and temporal distributions of ambient aerosol as a function of size and composition in order to better understand potential climate forcings. One approach to measure aerosol sources was installing instruments at large anthropogenic emitters like power plants and chemical manufacturers (Spurny 2005). In highly developed countries such as the United States spot monitoring is useful to enforce emission regulations. In 1998 a ground based global monitoring network, the Aerosol Robotic Network (AERONET), was introduced to expand the possible measurement locations (Holben et al. 1998). AERONET is a series of sun photometers placed around the globe to measure aerosol optical depth (AOD). AOD is a measure of the extinction of solar radiation by particles in the atmosphere. The quantity is dimensionless, corresponding to the amount of direct sunlight prevented from reaching the surface (Dutton et al. 1984). For the AERONET deployment of sun photometers a solar panel power source is used allowing access to remote locations providing data at sites beyond previous point source measurements. Extinction of the total air column is measured using the Sun for a source of light. Sun photometers operate over a number of wavelengths from visible to IR where the Sun has substantial intensity. Wavelengths where atmospheric gases such as water vapor absorb are excluded (Shaw 1983). Currently over 800 AERONET measurement points exist globally with ~25 existing over the ocean. This represents limitations of ground based measurements particularly since sea salt aerosol has high loading in the atmosphere as shown by Table 1.1 (Seinfeld and Pandis 2006). However, AERONET stations can continuously collect data at a specific location allowing for long term comparisons with high temporal resolution of measurements every 15 minutes during daylight (Kokhanovsky and de Leeuw 2009).

Further advancements in satellite capabilities since 1998 have provided for even greater spatial coverage of the Earth. Various instrument payloads exist on satellite platforms including Moderate Resolution Imaging Spectroradiometer (MODIS), Multiangle Imaging Spectroradiometer (MISR), and the Cloud-Aerosol Lidar with Orthogonal Polarization (CALIOP). In principle these instruments have similar operation to sun photometers in using the Sun as the source but differ by measuring reflection off the Earth's surface. For satellite based instruments reflectance is measured and an algorithm is used to match to a database of simulated reflectance values for various expected conditions (Levy et al. 2010). Space based spectrometers have an added advantage of measuring Sun intensity at the top of the atmosphere directly whereas ground based instruments must make assumptions to calculate a value by measuring over multiple angles (Kokhanovsky and de Leeuw 2009). Satellites have further improved the spatial coverage of aerosol loading providing measures of important phenomena such as long range transport (Zhang et al. 2017). Spatial resolution of satellites could be improved where MODIS for example only has on average 1 km resolution which misses fine structure of some point sources. The number of satellite payloads has increased in the past decade but for an individual instrument the temporal coverage of one location is challenging as most satellites must orbit the Earth limiting measurements to once per day at the same time of day for mid-latitudes. Future planned and recently launched geostationary satellites with aerosol monitoring payloads will improve temporal coverage.

In addition to the lack of spatial coverage for ground based instruments and the temporal coverage for space based instruments other inherent assumptions made in the calculations should be addressed to improve the ability to measure aerosol properties remotely. A few of these

challenges were outlined previously such as uncertainty in particle shape, CRI, and how atmospheric conditions such as relative humidity change these (Zhang et al. 2017). Additionally, the ability to make measurements on cloudy days is often times so challenging that those days are ignored from data sets (Zhang et al. 2017). The CRI is uncertain for some prevalent aerosol components over the entire wavelength range used by both ground and space based instruments making the determination of extinction difficult (Kokhanovsky and de Leeuw 2009). One recent study showed how errors in the assumed CRI for aerosol plumes located over Brazil led to MODIS overestimating the number concentration of accumulation mode particles (Levy et al. 2010). Others have suggested that aerosol growth through water uptake is poorly represented by look up algorithms used by satellites causing overestimations in number concentration (Shinozuka et al. 2015).

The work presented in this thesis is aimed at providing optical measurements for select aerosol components to expand the inventory of optical properties. Chapter 2 presents an iterative CRI retrieval algorithm for polystyrene spheres expanding the range of previously known values for aerosolized samples into UV wavelengths and Chapter 3 presents the measured optical extinction enhancement of montmorillonite as a function of water uptake for different aerosol generation methods.

CHAPTER 2

REFRACTIVE INDEX RETRIEVALS FOR POLYSTYRENE LATEX SPHERES IN THE SPECTRAL RANGE 220-420 NM

2.1 ACKNOWLEDGEMENTS

The work in this chapter was funded by the University of New Hampshire, College of Engineering and Physical Sciences. Data collection of extinction for PSL was done by Ryan T. Chartier. Compilation of the measured data and averaging of replicate trials was performed by Nicholas Levergood. A special thanks to J. Michel Flores for supplying the Igor Pro encoded retrieval algorithm. Finally, a thanks to Roger H. French for providing the numerical results for his 2007 publication used for comparison here. This chapter is reprinted with permission from Taylor and Francis.

2.2 INTRODUCTION

Aerosol interact with solar radiation directly through absorption and scattering as well as indirectly by acting as cloud condensation or ice nuclei (Charlson et al. 1992, IPCC 2013). Currently, the uncertainty associated with direct interactions limits the ability of models to accurately predict radiative forcing thus constraining improvements in our understanding of

climate change (IPCC 2013). Particle-light interactions depend on the wavelength of light, the size and shape of the particle, and the complex refractive index (CRI, $m = n \pm ik$) (Bohren and Huffman 1983). The CRI is a wavelength (λ) dependent physical property of each chemical species. The real portion of the refractive index (n_D) for some chemicals are reported in the CRC Handbook of Chemistry and Physics at $\lambda = 589$ nm, which is the sodium D-line denoted as the subscript (Haynes 2016). Other general references exist for n_D values, such as Lange's Handbook of Chemistry (Speight 2005), but complete CRI are usually reported in the literature only as a result of specific experiments and even then are limited. Despite being more common, n_D values are still not available within these reference books for some common chemicals present in ambient aerosols such as malonic acid, adipic acid, and pyrene (Rogge et al. 1993). In some cases the range of CRI for a chemical has been expanded by applying the Cauchy dispersion equation. This equation relates the wavelength of light to the real portion of the CRI through a series of constants which are characteristic of the chemical. While the theoretical basis of the equation no longer holds true, calculated indices in regions of normal dispersion are still satisfactory (Jenkins and White 2001).

Knowledge of the CRI, along with the size distribution and shape, of a type of aerosol are used to predict the influence on Earth's energy balance by calculating the single scattering albedo (SSA). Particularly the CRI provides information on the scattering and absorption ability of a type of aerosol. SSA is a ratio of the scattered light to the total attenuance where the dividing line between cooling and warming aerosol is 0.85 (Hansen et al. 1980, Ackerman and Toon 1981). Pure scatterers like particles composed of ammonium sulfate have a value of $k = 1x10^{-7}$ in the visible region and represent aerosol that would have an SSA > 0.85 and a net cooling effect on

the atmosphere (Toon et al. 1976, Charlson et al. 1991). Particles composed of black carbon have a higher value of k, reported in the literature as k = 0.63-0.79 at λ = 550 nm, resulting in the absorption of solar radiation, an SSA < 0.85, and ultimately a net warming effect (Bond and Bergstrom 2006). Often the CRI for specific chemicals, or types of aerosol, is only reported at a single wavelength, is only reported for n_D, or may even be unknown and thus climate impact is uncertain.

Measurement, or retrieval, of CRIs or portions of the CRI has been done in several ways. For example, ellipsometry can be used to directly determine the CRI by collecting an aerosol sample to be prepared into a thin film where a change in polarization of light reflecting off the surface of the film is measured (Humlicek 2005, Liu et al. 2013). Another method for determining the CRI is through retrievals from other optical properties. In specific, Lack et al. (2006) describes an experiment where: 1) the aerosol extinction was measured with cavity ring-down spectroscopy (CRD) and absorption was measured with photoacoustic spectroscopy (PAS) for absorbing nigrosin particles at a series of sizes, 2) the CRI was retrieved exclusively from the extinction efficiency results and then 3) a Mie theory curve was generated from the retrieved CRI to compare with the measured absorption cross section. The agreement is very good between the Mie Theory based on extinction retrieved CRI and the PAS measured absorption data (Lack et al. 2006). Others have followed a similar procedure for retrieving CRI for absorbing and non-absorbing aerosol which compare favorably with other methods and literature values (Abo Riziq et al. 2007, Spindler et al. 2007, Dinar et al. 2008, Freedman et al. 2009, Lang-Yona et al. 2009, Kim et al. 2010, Mack et al. 2010, Miles et al. 2010, Miles et al. 2010, Erlick et al. 2011, Bluvshtein et al. 2012, Washenfelder et al. 2013, Flores et al. 2014). For individual refractive

index components, the Abbe refractometer has been used to determine the real portion, n, of the refractive index for chemical samples by measuring diffraction of light traveling through two prisms sandwiching the sample. The imaginary part of the refractive index, k, describes light absorption by the bulk through the relationship to the absorption coefficient (Horvath 1993, Sun et al. 2007, Moosmuller et al. 2009). The absorption coefficient has been measured in many ways and these techniques have been reviewed recently and include the following instruments: aethalometer, particle soot absorption photometer (PSAP), micro soot sensor, multi-angle absorption photometer (MAAP), multi-filter rotating shadowband radiometer, PAS, single particle soot photometer (SP2), integrating sphere, plate or sandwich, and the subtraction method via extinction and scattering measurements (Horvath 1993, Moosmuller et al. 2009). A number of these instruments and techniques have potential filter interference requiring corrections, complicated sample preparation requirements and/or operate at a single or limited number of wavelengths.

The development of a broadband aerosol extinction differential optical absorption spectrometer (AE-DOAS) has allowed for the measurement of light extinction by aerosol over the spectral range of 220-1050 nm, with optimal results from 235-700 nm (Chartier and Greenslade 2012). The AE-DOAS can be used for the retrieval of CRI over nearly the entire solar spectrum when coupled with Mie Theory and an iterative minimization routine. To validate this application, measurements of extinction were made for polystyrene latex spheres (PSL), a common standard used to calibrate aerosol research instruments. PSLs are widely used since they are manufactured to be spherical and of a known diameter allowing Mie Theory to accurately predict extinction cross sections. The AE-DOAS measures extinction, so it is important to measure multiple

diameters in order to minimize the uncertainty on the retrieved values, as scattering and absorption can respond differently to changes in particle size (Zarzana et al. 2014). The measurement of extinction alone represents a limitation to instruments like the AE-DOAS or CRD in retrieving the CRI. To the best of our knowledge only French et al. have previously measured the CRI of thin film polystyrene below 360 nm (French et al. 2007). Washenfelder et al. (2013) retrieved CRI for polystyrene spheres between 360-420 nm based on similar optical measurements and Ma et al. measured suspensions of polystyrene spheres in water from 370-1610 nm (Ma et al. 2003). Two other recent studies retrieved CRI outside of the wavelength range presented in this work, specifically in the visible and IR regions with references to additional studies contained within (Miles et al. 2010, Zhao et al. 2014).

In this chapter, retrieved CRI values are presented for PSLs in the wavelength range from 220-420 nm, larger uncertainties are expected where there is less lamp intensity below 235 nm. Further, the relationship between particle diameter and wavelength of light is investigated with respect to the retrievals, where the differences between Rayleigh and Mie scattering become important at small particle diameters.

2.3 EXPERIMENTAL

2.3.1 AE-DOAS Instrument Description

The AE-DOAS manufactured by Cerex Monitoring Solutions (CMS UV-5000) consists of a xenon lamp and a detector as part of a standard UV-Vis spectrometer, plus a white-type

multi-pass gas cell (Chartier and Greenslade 2012). The Xe lamp produces photons spanning the range from the ultraviolet to near infrared (~220-1050 nm). The emission intensity of this lamp has a large broad peak, with substantial intensity from 275-800 nm. Lower energy wavelengths in the IR are characterized by sharp and intense emission peaks making this wavelength range challenging for measurement. Lamp variability can have a substantial effect on the measured extinction, but this variability is more significant from day to day as opposed to over the time of an experiment (Jordan et al. 2015). In this work, the 220-420 nm range is used and deviations in lamp intensity are minimized by using background measurements made before sampling. In a recent redesign of the AE-DOAS, which has also been referred to as the Spectral Aerosol Extinction (SpEx) instrument, higher flow rates are used to exchange the volume within the gas cell in as little as 40 s. In addition, backgrounds are taken both before and after sampling to better understand any lamp drift, where these modifications could be used in future AE-DOAS experiments (Jordan et al. 2015).

In more detail, the optical cell contains one fixed (primary) and two movable (secondary) concave mirrors of equal curvature. Slight adjustments, of the secondary mirrors, allow for the path length to range in 2.44 m increments from 2.44 to 19.51 m by changing the number of internal reflections within the cell. These mirrors are not protected by any purge flow avoiding dilution corrections but degradation of mirror reflectivity could introduce uncertainty to measurements. This is minimized with the timing of the background measurements. The cell is made from stainless steel with dimensions of 73.0 cm x 19.2 cm x 7.5 cm creating an internal volume of around 5.8 L; it was kept grounded during experiments. Finally, the spectrometer detector consists of a grating and a 3078 linear diode array. Fiber optic cables (Ocean Optics

QP600-2-SR-BX) connect the gas cell to the lamp and spectrometer. For a more detailed explanation of instrumental design and validation, see previous work by Chartier and Greenslade (2012).

2.3.2 Sample Generation and Extinction Measurement

Samples were prepared from 10 % (w/w) polystyrene latex sphere suspensions (Thermo Scientific, formerly Duke Scientific) by further diluting 15 drops with 20 mL of deionized water (J. T. Baker, HPLC water). PSLs of five different sizes were used for the experiment including diameters (*d*) of 150 (3150A), 220 (HF22), 300 (HF30, 5030A), 430 (5043A), and 600 (5060A) nm. No attempts were made to remove the proprietary surfactant included during manufacturing. The sample is aerosolized in a Collison-type atomizer using nitrogen (N_2) gas (May 1973, Liu and Lee 1975). The aerosol generation and further experimental design are depicted in Figure 2.1. This aerosol entrained in nitrogen is dried to a relative humidity of < 3 % by passing over molecular sieves housed in a diffusion drier before entering into a differential mobility analyzer (DMA, TSI model 3080L). Within the DMA, a minimally polydisperse aerosol sample is refined by first establishing a charge on the particles with a krypton source and then separating by electrical mobility within a concentric electric field between an inner rod and outer cylinder. Corrections for multiply charged particles exiting the DMA typically need to be applied to the particle number concentrations and the extinction results; however in this case, due to the nature of the sample, such a correction is not applied.

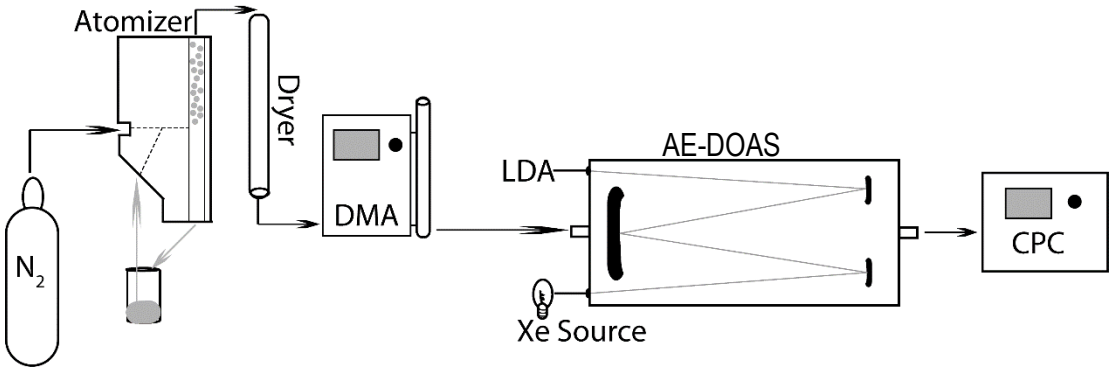

Figure 2.1. The complete experimental design used for broadband extinction measurements. The path through the system starts on the left with aerosol generation from a sample solution using nitrogen in an atomizer block. The aerosol is then dried before size selection with a DMA. Optical extinction is measured next with the AE-DOAS and finally number concentration is measured with the CPC. The abbreviations used are: DMA - differential mobility analyzer, AE-DOAS - aerosol extinction differential optical absorption spectrometer, LDA - linear diode array, Xe source – xenon lamp, CPC - condensation particle counter.

Further information on multiply charged PSL particle and DMA size selection is included in the results section. This now monodisperse aerosol sample enters into the AE-DOAS where extinction is continuously measured. For these experiments, the AE-DOAS was operated at a path length between 17.08 and 19.51 m. The flow of aerosol then exits the cell and terminates at a condensation particle counter (CPC, TSI model 3775) where concentration is measured. The CPC has an uncertainty of ±10 % and this dominates the uncertainty of the extinction cross section measurements. The aerosol flow within the DMA, AE-DOAS, and CPC is kept at 0.3 L/min to promote laminar flow within the setup. Importantly, a time offset between the AE-DOAS and the CPC is determined. This is done by correlating the highest concentration measured with the CPC to the highest extinction measured with the AE-DOAS, and applying this time offset to all other measurements; the observed offset agrees with times estimated from the flow and instrument dimensions between the two locations. Typically, an experiment takes about an hour from measuring the blank before sample to purging the cell of aerosol following measurement.

2.4 RESULTS

Collected data from individual experiments includes light intensity measurements of dry, filtered, particle free nitrogen gas from within the gas cell for background (I_0) and of the aerosol sample (I), as well as aerosol number concentration (N). Aerosol size is controlled by manufacturing and DMA selection. This data allows for the determination of experimental extinction cross sections, C_{ext} (cm^2/particle), which can be compared to Mie Theory based calculations. First experimental extinction, σ_{ext} (cm^{-1}), is calculated using Equation (2.1) where l is the path length.

$$\sigma_{ext} = \frac{-\ln\left(I/I_0\right)}{l} \tag{2.1}$$

Extinction cross sections (C_{ext}) are then calculated using the number concentration, N (particles/cm^3), from the CPC using Equation (2.2). Number concentrations are found by averaging 2.5 minutes of data from the CPC which corresponds to the time for the AE-DOAS to collect the light intensity data. Since there is an offset between intensity and concentration measurements from the travel time of the aerosol, a time offset described above is used. An experimentally obtained spectrum of the measured extinction cross section for PSLs with a diameter of 150 nm is represented by the open grey circles in Figure 2.2.

$$C_{ext} = \frac{\sigma_{ext}}{N} \tag{2.2}$$

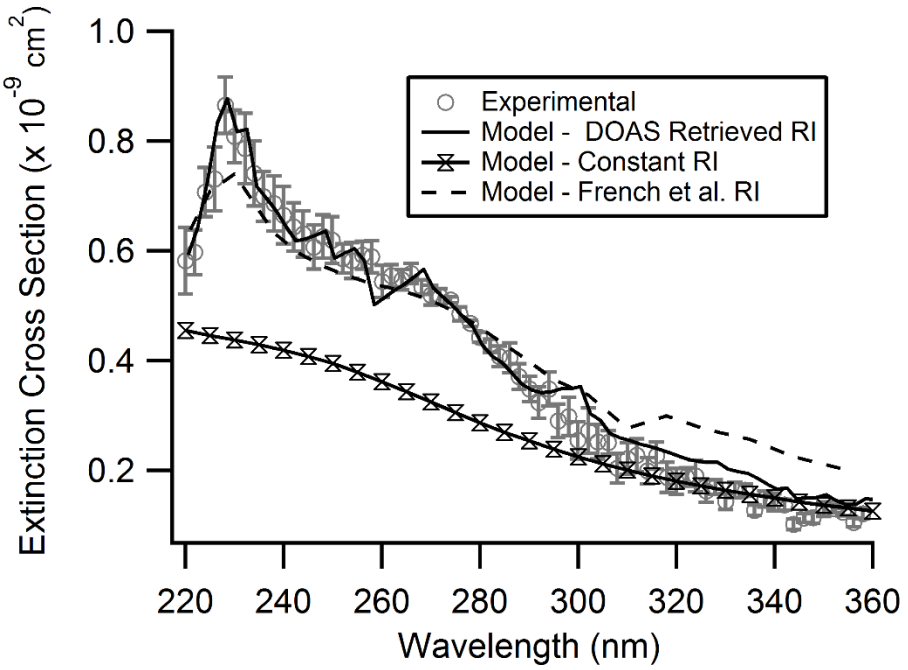

Figure 2.2. The measured extinction cross section for 150 nm PSLs using the AE-DOAS shown as open grey circles. The error bars on the measured values represent 1 σ of the mean. Shown for comparison are Mie Theory calculations based on various CRI. The solid black line represents the CRI retrieved in this manuscript, the dashed black line represents the CRI for polystyrene-568 measured by French et al. (2007), and the open hour glasses represent a constant RI supplied by the manufacturer at the wavelength of 589 nm. Points are connected by lines to guide the eye where the French et al. (2007) data is reported at larger intervals than the AE-DOAS data.

In addition, the dimensionless extinction efficiency, Q_{ext}, is calculated for use in the CRI retrievals. A graph of this quantity versus the dimensionless size parameter (χ) produces a uniquely shaped curve that is distinctive for different CRI. The size parameter, defined as $\pi d/\lambda$, is useful when comparing the extinction of two spheres with the same CRI. Even if the spheres have different diameters as long as χ is the same, the extinction efficiency will be equal. Q_{ext} is calculated using Equation (2.3) below where r (cm) is the radius of the particle.

$$Q_{ext} = \frac{C_{ext}}{\pi r^2} \tag{2.3}$$

Final manipulation of the data includes averaging Q_{ext} for replicate trials as well as calculating the standard deviation on Q_{ext} for each diameter. The number of trials and the experimental path lengths for each sized PSL are shown in Table 2.1.

Table 2.1. Path length and number of trials averaged to calculate Q_{ext} for the various sized PSLs. The uncertainty on the diameter of the PSL in solution ranges from ≤ 3 % to ≤ 5 %. Fewer trials of 600 nm spheres were completed as it was more challenging to obtain the necessary particle number concentration.

Sphere Diameter (nm)	Path Length (m)	# of Trials
150	19.51	4
220	19.51	4
300	17.08	5
430	19.51	8
600	19.51	2

The experimental Q_{ext} average and standard deviation along with the sphere diameter and size uncertainty from the manufacturer are used for the retrieval algorithm (Washenfelder et al. 2013). This algorithm compares the measured extinction efficiency calculated with Equations (2.1)-(2.3) to those calculated with Mie Theory for a particular CRI (Washenfelder et al. 2013). Both the real and imaginary portions of the CRI are varied within the retrieval to minimize the χ^2 in Equation (2.4), where N_{Dp} is an index for a particular PSL diameter, Q_{ext} is the experimental extinction efficiency, and Q_{Mie} is the calculated Mie Theory extinction efficiency for some CRI:

$$\chi^2 = \sum_{i=1}^{N_{Dp}} \left(\frac{Q_{ext} - Q_{Mie}}{Q_{ext}} \right)_i^2 . \quad (2.4)$$

The uncertainty in the retrieved real and imaginary portions of the CRI is obtained empirically by considering the range of Q_{ext} values bounded by the uncertainty, which is on average ±11 %

of Q_{ext}; the method used here is based on that described by (Washenfelder et al. 2013). This retrieval is repeated for the wavelength range 220-420 nm in 2 nm steps.

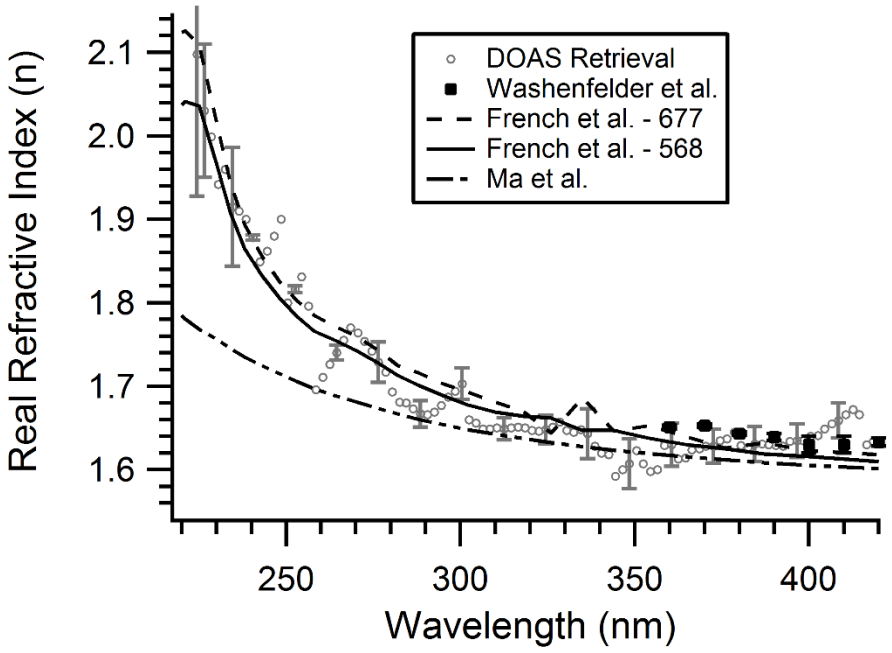

Figure 2.3. The real portion (n) of the CRI versus wavelength retrieved from this work with literature values. The open grey circles represent the retrieved values from the AE-DOAS with error bars representing the retrieval uncertainty, the solid black squares represent the data from Washenfelder et al. (2013), the dashed line represents polystyrene-677 from French et al. (2007), the solid black line represents polystyrene-568 from French et al. (2007), and the dashed-dotted line represents the values generated from the Cauchy coefficients extrapolated below 370 nm from Ma et al. (2003). Lines are used for the French et al. (2007) and Ma et al. (2003) data to guide the eye where data is available at larger intervals than the AE-DOAS data. Numerical values and uncertainties for the retrieved refractive index are presented in Table A1 in the appendix, where only a subset of uncertainties are presented here for clarity.

The retrieved CRI values and uncertainties are given in Table A1 in the appendix and are displayed graphically in Figures 2.3 (for the real portion (n)) and 2.4 (for the imaginary portion (k)). When using a DMA to size select particles for optical measurements, it is generally necessary to correct for multiply charged particles where larger sizes would have a similar mobility ratio so they could pass through the DMA and contribute to the observed number concentration and optical extinction (Hoppel 1978).

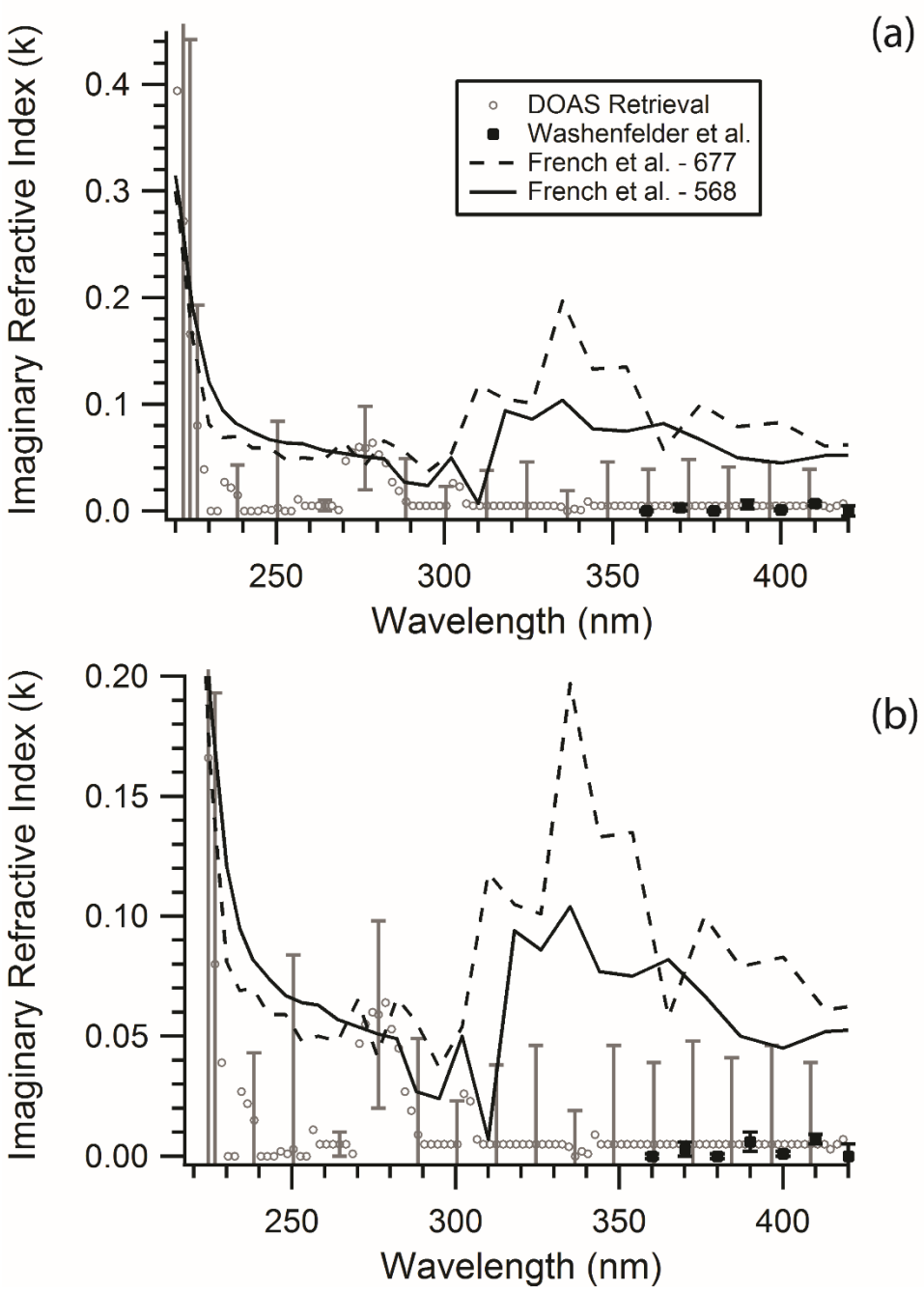

Figure 2.4. (a) - The imaginary portion (k) of the CRI versus wavelength retrieved from this work with literature values. The open grey circles represent the retrieved values from the AE-DOAS with error bars representing the retrieval uncertainty, the solid black squares represent the data from Washenfelder et al. (2013), the dashed line represents polystyrene-677 from French et al. (2007), and the solid black line represents polystyrene-568 from French et al. (2007). Lines are used for the French et al. (2007) data to guide the eye. (b) - An expanded view of panel (a) in the wavelength range from 240-420 nm to show detail. Only ~20 % of the data is shown with error bars for clarity. Numerical values and uncertainties for the retrieved refractive index are presented in Table A1 in the appendix.

Several literature reports have been considered on the necessity of such corrections for PSL in analyzing the results. A two DMA method has been used to show polydisperse samples like ammonium sulfate can have measured extinction cross sections 17-47 % greater than those predicted with Mie Theory whereas PSLs are typically only 2-12 % greater (Khalizov et al. 2009). This small difference for PSLs was hypothesized to result from surfactant residue which prevents agglomeration and minimizes doublets but may yield small changes in diameter (Khalizov et al. 2009). Other researchers have noted that PSL conglomerates were observed in experiments, but when simplified and advanced correction approaches were compared, no systematic differences were observed (Petzold et al. 2013).

Further, high linear correlation between Mie Theory including number concentration data and experimentally measured extinction values were observed yielding slopes between the two correction methods which were not statistically different, thus it was concluded no corrections were needed (Petzold et al. 2013). Another report noted that the DMA in use for the experiment removed aggregate and surfactant particles from the optically interrogated flow (Miles et al. 2010). Ultimately, PSLs are nearly monodisperse with a size distribution smaller than the DMA transfer function, they contain surfactant to prevent aggregation, and other researchers have noted low impact to their data from multiply charged particles, therefore corrections are not applied for multiply charged particles in this work (Khalizov et al. 2009, Miles et al. 2010, Petzold et al. 2013).

Coefficients (A, B, and C) for the Cauchy dispersion equation were found using Equation (2.5) where λ is the wavelength in microns and $n(\lambda)$ is the real refractive index at that λ:

$$n(\lambda) = A + \frac{B}{\lambda^2} + \frac{C}{\lambda^4}. \quad (2.5)$$

The retrieved PSL real refractive index data from Table A1 in the appendix is fit to Equation (2.5) using an iterative χ^2 minimization in Igor Pro. The resulting Cauchy coefficients are given in Table 2.2 with values from the literature for comparison. Others have published results for similar relationships such as the Cauchy relationship based on a few wavelengths, a modified Cauchy relationship with additional coefficients, or Sellmeier's formula. A recent and comprehensive review of the literature can be found in Miles et al. (2010).

Table 2.2. Cauchy dispersion equation coefficients determined for polystyrene latex spheres based on fitting Equation (2.5). This work focuses on utilizing the retrieved real refractive index at UV-Vis wavelengths from 220-420 nm. Whereas, the Ma et al. (2003) values are based on the 390-1310 nm wavelength range and the Matheson and Saunderson (1952) values are based on measurements from 436-767 nm.

	This Work	Ma et al. (2003)	Matheson and Saunderson (1952)
A	1.538(11)	1.5725	1.5663
B (μm^2)	0.0043(16)	0.003108	0.00785
C (μm^4)	0.00094(5)	0.00034779	0.000334

2.5 DISCUSSION

The retrieved values of the real and imaginary CRI as a function of wavelength for PSL are shown in Figures 2.3 and 2.4, respectively and Table A1. In Figure 2.3, the real portion (n) shows normal dispersion by an increase in the index with increasing energy (Bohren and Huffman 1983). Agreement with previous literature results is also shown for most regions of the spectrum. This is especially true for the Washenfelder et al. (2013) data which uses a similar

technique to that presented here. Briefly, Washenfelder et al. (2013) aerosolized PSLs and measured extinction with either a custom broadband cavity enhanced spectrometer (BBCES) or a CRD both of which are similar to our optical interrogation of suspended PSL but differ in the wavelengths available for measurement. The French et al. (2007) results also show general agreement for the real portion over the spectrum. That study employed spectroscopic ellipsometry to interrogate thin films of two different formulations of polystyrene. These two formulations of the polymer return CRI values with some differences suggesting that if the PSLs used in this work, or by Washenfelder et al. (2013), are a different formulation, then differences would be observed (Liu et al. 2013). Further, the manufacturer of the PSLs uses a proprietary surfactant which may stay on the surface of the aerosols after generation and this may contribute to the CRI retrieved in this work (Khalizov et al. 2009). The Ma et al. (2003) data shows more deviation compared with all three studies, particularly below $\lambda = 300$ nm. It is important to note that the data from Ma et al. (2003) has been extrapolated beyond the intended region which ends at $\lambda = 390$ nm using the reported Cauchy coefficients and the agreement with other data sets is good from 390-420 nm. To improve the accuracy of the Cauchy model for PSLs based on the newly retrieved real refractive index at UV wavelengths, new coefficients have been calculated and are shown in Table 2.2. The values compare well with the literature. The differences in coefficients may result from the significant increase in $n(\lambda)$ into the UV observed in Figure 2.3 and the different wavelength ranges considered. Further, the Ma et al. (2003) results may also differ because solution phase measurements of suspended PSLs were the basis of the coefficient determination and solvent effects may be possible. Whereas, the Matheson and Saunderson (1952) work was completed by measuring the diffraction of light through polystyrene prisms and are bulk measurements.

In Figure 2.4, the retrieved imaginary portion of the CRI shows excellent agreement with the similar work of Washenfelder et al. (2013). The uncertainty on a number of these retrieved values is larger than the values suggesting that the $k + \Delta k$ represents an upper limit for k. Future refinements to k values for PSL in this wavelength region may benefit from a supplementary absorption measurement. PSLs show two absorption bands, one below $\lambda = 240$ nm and one centered at $\lambda = 280$ nm. While these compare well with the imaginary portion measured by French et al. (2007) the band centered at 280 nm may also be a result of additional gas phase absorption, mainly acetone, which was found to occasionally persist in the lab during measurement. There are noticeable differences however between the polymers of French et al. (2007) and this work. The disagreement is increased at wavelengths greater than 300 nm and is most likely caused by differences in the techniques used or the polymer formulation, as discussed above. With regard to the technique, French et al. (2007) note that based on spectral differences for a single polystyrene film measured with two different spectroscopic techniques used in the study, the uncertainty of the imaginary portion is quite large at the absorption maximum and could be at other wavelengths as well. The authors also demonstrate that absorption spectra have differences between bulk and surface sampling. The films used by French et al. (2007) may not replicate the same surface to bulk ratio of the PSLs causing the measured values to disagree. A final consideration is that birefringence, a measure of how the CRI varies with the direction of light propagation, has been shown to increase for polystyrene in the visible region with decreasing wavelength (Inoue et al. 1998). The birefringence is induced by strain from preparing the material and may not be the same between the films used by French et al. (2007) and the PSLs used here.

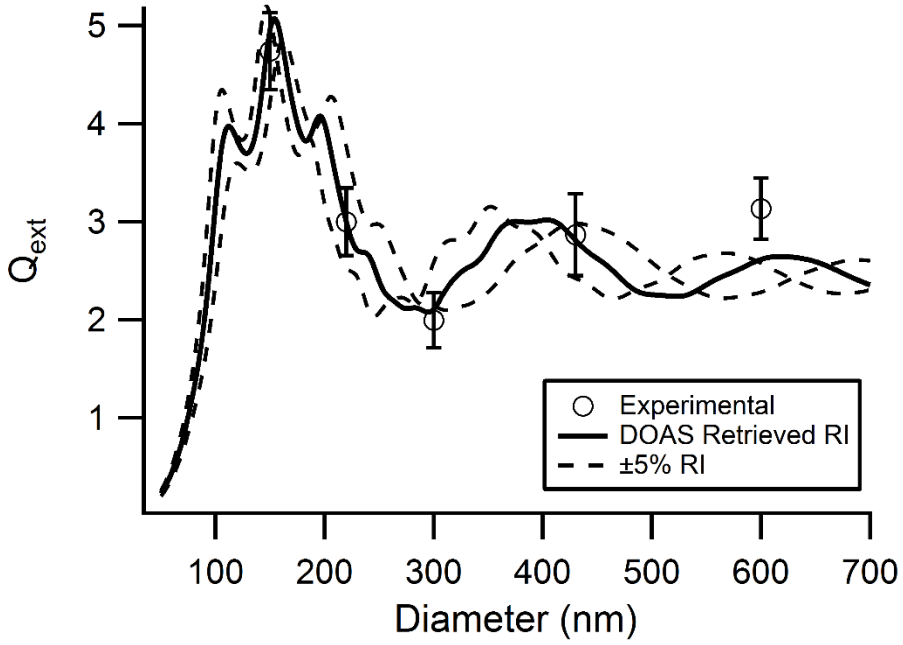

Figure 2.5. Extinction efficiency versus diameter for PSLs measured at λ = 228 nm with the AE-DOAS. The open circles represent the measured values with errors bars representing 1 σ of the mean, the solid black line is the Mie Theory extinction calculated using the retrieved CRI from this work, and the dashed line represents Mie Theory extinction calculated for ±5 % of both portions of the retrieved CRI.

The diameter of the PSLs is an important variable depending on the wavelength of interest for a CRI retrieval. The uncertainty of the retrieved values generally increases as the wavelength of light decreases particularly into the UV region as seen in Figures 2.3 and 2.4. This increase in the uncertainty magnitude can be explained using a different representation of the experimental data. Here, Figures 2.5 and 2.6 show a comparison of the measured extinction efficiency (Q_{ext}) for PSLs and calculated Mie Theory extinction efficiency (Q_{Mie}) for the retrieved CRI values versus particle diameter at two different wavelengths, 228 and 351 nm, respectively. In both Figures 2.5 and 2.6, the measured Q_{ext} values are represented by open circles and the calculated Mie Theory model using the retrieved CRI is shown with a solid black line. Also included are two other Mie Theory models, shown as dashed lines calculated using ±5 % of both portions of the retrieved CRI. While Q_{ext} agrees with the model at λ = 228 nm better than at λ = 351 nm based off visual

inspection, the resulting uncertainty of the retrieved real portion of the CRI for 228 nm is 0.04 which is greater than the uncertainty for 351 nm, 0.03.

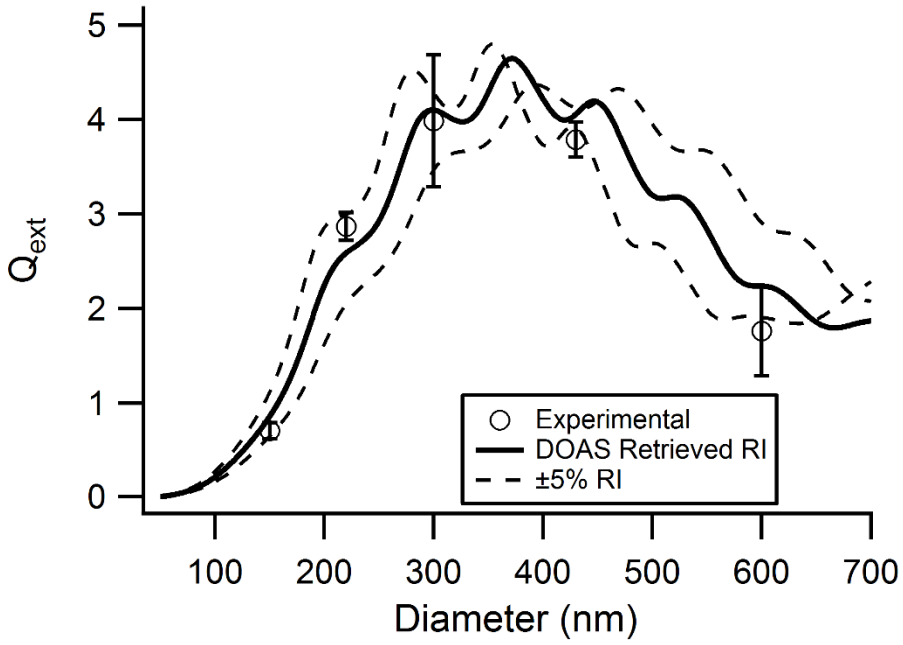

Figure 2.6. Extinction efficiency versus diameter for PSLs measured at λ = 351 nm with the AE-DOAS. The open circles represent the measured values with errors bars representing 1 σ of the mean, the solid black line is the Mie Theory extinction calculated using the retrieved CRI from this work, and the dashed line represents Mie Theory extinction calculated for ±5 % of both portions of the retrieved CRI.

This is due to the fact that for each λ, the Q_{ext} becomes more sensitive to small changes of the CRI as the particle size decreases reflected by the decreasing area between the dashed lines towards the smallest diameters in Figures 2.5 and 2.6. In order to improve the precision of the retrieved CRI, it is crucial to select particles with diameters in the steep beginning portion of the curve where the variability in CRI causes only small differences in the calculated Q_{ext}. For example, at λ = 228 nm, the PSL diameters chosen for this experiment do not fall in the steep portion of the curve before d = 110 nm whereas at λ = 351 nm three of the particle diameters measured fall in this region. In this work, the extinction measurements were always completed

with the same particle diameters no matter the wavelength of interest. By failing to choose sizes in the steep region, the retrieved CRI will have more uncertainty thus our results yield increases in both portions of the CRI uncertainty with decreasing wavelength. Previous literature has shown that careful selection of particle diameters allows for increased precision in retrieval of CRI with as few as two diameters (Bluvshtein et al. 2012).

This research on PSLs demonstrates how much the CRI can vary over a range of wavelengths. The CRI variation with λ will have a large impact on light extinction as shown in Figure 2.2. Specifically, when using the $n_D = 1.59$ as supplied by the manufacturer at other wavelengths there is quite poor agreement between model and experiment. The model agreement looks good at wavelengths longer than 300 nm, but then begins deviating at shorter wavelengths and clearly fails to reproduce the peak in the experimental data around 220 nm. This demonstrates a need to measure the CRI for atmospherically relevant aerosol chemicals particularly in the UV region. In the visible region, it is generally the case that the variation in CRI is much less. However, at $\lambda = 420$ nm near the division between visible and UV regions, while the retrieved CRI from this work, n = 1.64, is only different from the manufacturer constant n_D by 3 %, the Mie Theory modeled extinction cross section varies by 5-20 % depending on the particle diameter. Since the solar spectrum peaks within the visible region and still has significant intensity at wavelengths around 420 nm, this is further evidence that limited knowledge of the CRI can contribute added uncertainty in model predictions of radiative forcing.

The AE-DOAS expands the wavelength range accessible for aerosol extinction measurements into the UV to 220 nm. For the wavelength range from 235-700 nm, the AE-DOAS average

detection limit based on 3σ baseline noise is 32.5 Mm^{-1} for a 3 minute average with an order of magnitude better detection limit at specific wavelengths. A few of the other instruments which have different advantages but have been designed and used for aerosol extinction measurements are discussed here for comparison. CRD instruments can use a variety of laser sources to measure aerosol extinction including but not limited to an Nd:YAG at λ = 355, 532, and/or 1064 nm (Sappey et al. 1998, Smith and Atkinson 2001). CRD is incredibly sensitive and time responsive with detection limits around 0.17 Mm^{-1} per second average owing to the long path lengths and fast lasers (Pettersson et al. 2004). Washenfelder et al. (2013) developed a broadband cavity enhanced instrument, the BBCES, which measures aerosol extinction in the wavelength ranges from 360-390 nm and 385-425 nm with a precision of ~0.19 Mm^{-1} for 1 minute averages at the central wavelengths of 365 and 405 nm, respectively. The CAPS PM_{ex} instrument is based on the cavity attenuated phase shift technique and operates at 630 nm (and other wavelengths, see Massoli et al. (2010)) with a detection limit of less than 0.3 Mm^{-1} for 60 second averaging (Kebabian and Freedman 2007, Kebabian et al. 2007). BBCES, CAPS PM_{ex} and CRD all have versions or were specifically designed for field measurements (Baynard et al. 2007, Petzold et al. 2013, Washenfelder et al. 2013). Still other instruments exist for laboratory measurements of aerosol extinction and were discussed in a previous paper (Chartier and Greenslade 2012). The AE-DOAS is unique because it expands extinction data collection and the potential for subsequent CRI retrieval further into the UV than any of these other instruments and provides closer to continuous spectral results.

In conclusion, the ability of the AE-DOAS to retrieve CRI values at wavelengths from the visible into the UV for PSLs has been shown with good agreement to similar measurements by other

researchers. Importantly the wavelength range of known PSLs CRI values has been extended further into the UV. With regards to PSL characterization, these new results should allow for more accurate calibrations when used as a standard for a variety of optical measurements. It's noted that some differences in CRI may arise due to differences in material and our work is specifically concerned with commercially available polystyrene spheres.

In the future, this instrument can be used to optically characterize an expanded range of atmospherically relevant aerosol especially into the UV where work by others indicates light absorption by carbonaceous and secondary organic species (Hecobian et al. 2010, Flores et al. 2014). The ability of the AE-DOAS to retrieve CRI allows the balance between scattering and absorption to be quantified and the warming or cooling of a particular aerosol species to be assessed.

CHAPTER 3

MINERAL DUST AEROSOL WATER ADSORPTION MEASURED OPTICALLY WITH CAVITY RING-DOWN SPECTROSCOPY: A COMPARSION BETWEEN DIFFERENT AEROSOL GENERATION METHODS

3.1 ACKNOWLEDGEMENTS

The work in this chapter was funded by the University of New Hampshire, College of Engineering and Physical Sciences and Chemistry Department. Dry generation was developed for our group by Jillian Morang based on the work of Garimella et al. (2014) and she participated in data collection.

3.2 INTRODUCTION

Mineral dust is a common component of atmospheric aerosol contributing around 25 % of the total yearly emitted mass, at 2,980 Tg, as well as a similar fraction to total atmospheric loading (Seinfeld and Pandis 2006, Zhang et al. 2012, IPCC 2013). Further, the amount of dust is expected to rise in the 21st century from desertification caused by changes to land use and climate (Prospero and Lamb 2003). Entrained mineral dust aerosols interact with light, thus contributing to radiative forcing (RF), a measure of the change in incoming minus outgoing irradiance often used to quantify a contribution to climate change. Mineral dust aerosol is made

up of clays, carbonates, iron oxides, and quartz with ratios dependent on the source (Prospero 1999, Lafon et al. 2006). The clay portion of mineral dust aerosol has been shown in laboratory experiments to swell in the presence of water vapor (Herich et al. 2009, Koehler et al. 2009), and the swelling enhances light interaction (Attwood and Greenslade 2011) as has been observed in the atmosphere (Carrico et al. 2003, Lack et al. 2009). Recent studies have shown the method used to generate clay and mineral dust samples in laboratory experiments can affect the measured results (Kumar et al. 2009, Sullivan et al. 2010, Garimella et al. 2014). Differences observed in these studies could be linked to observations that suspension derived clay aerosol samples are difficult to dry, especially the complete removal of interlayer water (Mooney et al. 1952, Cases et al. 1992). The typical low concentration of clay in the suspension used to generate aerosol results in a large amount of interlayer water (Norrish 1954, Svensson and Hansen 2013). As such, our work focuses on measuring light extinction enhancement as a function of relative humidity for montmorillonite aerosols wet generated from variable concentrated suspensions, as well as dry generated from powder, to investigate a concentration effect on water swelling.

Atmospheric dust originates from the arid and semiarid regions of the world where important factors such as wind friction speed, vegetation cover, and soil moisture content affect the total burden (Zender et al. 2003, Seinfeld and Pandis 2006). Dust particles are injected into the atmosphere when wind blowing over the surface initiates the process of saltation. Due to high cohesion forces between individual particles in the soil, only large particles (d > 60 μm) are initially mobilized. These particles are so massive they fall quickly, generating longer lived aerosol by bombarding and sandblasting the surface, lofting smaller particles into the boundary layer (Alfaro and Gomes 2001, Zender et al. 2003). The smaller range of particles (< 1 μm) have

lifetimes on the order of a week allowing for long range transport around the globe during which particles encounter many different atmospheric conditions (Prospero 1999, Gong et al. 2006, Schepanski et al. 2009, Uno et al. 2009, Huneeus et al. 2011, Yu et al. 2012, Achakulwisut et al. 2017). One example is Saharan dust transported across the Atlantic Ocean from Africa to the Caribbean and Eastern United States (Prospero 1999, Schepanski et al. 2009). Similarly Asian dust has been shown to travel across the Pacific Ocean to the Western United States, and even circumnavigate the Earth (Gong et al. 2006, Uno et al. 2009, Yu et al. 2012, Achakulwisut et al. 2017).

In terms of chemical composition, the clay portion of mineral dust aerosol contains aluminum and silicon. These elements coordinate to oxygen and form negatively charged repeating layers held together by van der Waals forces and interlayer charge countering cations such as Na^{+}, Ca^{2+}, and Mg^{2+}. One type of clay is montmorillonite, formed from the weathering of volcanic material (Chester et al. 1972). Montmorillonite is a minor component of the total clay burden accounting for an average of ~20 % with the highest concentrations found at low latitudes (Chester et al. 1972). Since adjacent montmorillonite aluminosilicate layers are weakly bound together through electrostatic interactions, water can penetrate into the interlamellar space and push the layers apart allowing the structure to swell (Brindly and Brown 1984).

For montmorillonite, the amount of water within the structure is dependent on the properties of the interlayer cations such as hydration energy, charge, and size (Brindly and Brown 1984, Hensen and Smit 2002). The swelling of montmorillonite is determined by assessing if the energy released by hydrating a cation is greater than the attractive force between the cation and

the negatively charged aluminosilicate layers (Norrish 1954, Brindly and Brown 1984, Hsiao and Hedström 2017). If the process is energetically favorable, water will penetrate between the layers to hydrate additional cations resulting in the layers pushing apart (Grim 1962, Brindly and Brown 1984). For example, the cations Ca^{2+} and Na^{+} have similar ionic radii, but since divalent Ca^{2+} has twice the charge of monovalent Na^{+}, Coulomb's Law predicts a stronger attractive force to overcome for Ca^{2+} rich montmorillonite. However, divalent cations typically have larger hydration energies compared to monovalent cations (424 and 1616 kJ/mol for Na^{+} and Ca^{2+}, respectively) (Norrish 1954). Ultimately, previous studies have measured increased water uptake for Na-montmorillonite compared to Ca-montmorillonite demonstrating the overall effect of the competing energetics (Norrish 1954, Brindly and Brown 1984). Natural samples of montmorillonite are likely to contain a mixture of cations in unknown or variable concentration which could result in observed differences in experimental water uptake measurements.

Previous studies have shown that the generation method used to prepare laboratory mineral aerosol alters water uptake measurements (Sullivan et al. 2010, Kumar et al. 2011, Garimella et al. 2014). Those authors measured cloud condensation nuclei (CCN) activity at supersaturated conditions for aerosols generated with two methods, one from suspension of mineral in water, referred to as wet generation, and one from powder, referred to as dry generation. In all cases, the authors measured increased activity, indicating enhanced water uptake, for the wet generated particles compared to dry generated. Garimella et al. (2014) measured a difference in CCN activation between wet and dry generated Na-montmorillonite aerosol, hypothesizing the suspension used for wet generation allows for the interlayer cations to redistribute, resulting in enhanced water activity. Both Sullivan et al. (2010), using calcium mineral samples, and Kumar

et al. (2011), using montmorillonite samples, hypothesized artifacts are introduced to the mineral particles during wet generation, possibly water, resulting in a more wettable surface and thus enhanced water activity.

Retained water on wet generated mineral particles, especially montmorillonite, could be explained by the ineffectiveness of the commonly used room temperature diffusion dryer. Due to the nature of the montmorillonite structure, with water residing on the exterior surface as well as in between the layers, generating a water free sample requires the use of elevated temperature, use of vacuum, or long drying times (Mooney et al. 1952, Cases et al. 1992, Schuttlefield et al. 2007, Hatch et al. 2012). Specifically, Cases et al. (1992) studied the water content of bulk montmorillonite samples using controlled transformation rate thermal analysis, measuring mass loss as a function of temperature increase. At room temperature physically adsorbed water is removed efficiently from the clay surface (Cases et al. 1992). In order to remove the interlayer water hydrating the cations, in that case mostly Na^+ for Wyoming sourced montmorillonite, temperatures as high as 527 ºC were required (Cases et al. 1992). Diffusion dryers operated at room temperature have been used extensively to prepare dry aerosol samples from wet generation which may not remove all the interlayer water.

As mentioned previously, the amount of water contained within the montmorillonite structure is related to the types of interlayer cations present. Additionally, others have shown that when montmorillonite is in suspension, layer spacing, and therefore water content, is a function of the suspension concentration (Norrish 1954, Svensson and Hansen 2013). Svensson and Hansen (2013) used X-ray diffraction (XRD) to show that increasing the concentration of water in a

Na-montmorillonite suspension results in layer expansion. For suspensions made with low water content, 20 % (w/w), the authors measured layer spacing of 19 Å. Increasing the water concentration from 20 to 50, 70, and 90 % results in the layers expanding to separations of 45, 88, and 280 Å, respectively (Svensson and Hansen 2013). Both Kumar et al. (2011) and Garimella et al. (2014) used montmorillonite suspensions with high water concentration (> 90 %) and other concentrations were not reported. Upon atomization and drying, the swelling process demonstrated by the increased layer spacing may not be fully reversible and we hypothesize this would result in variable water content correlated with suspension concentration for laboratory generated aerosol samples.

Initial water content has been shown to be an important variable in other montmorillonite water activity studies. Mooney et al. (1952) used absorption gravimetry to measure the mass of water adsorbed by montmorillonite exposed to water vapor. Samples were prepared by drying the bulk powder at 70 ºC under high vacuum. The authors then cycled the sample through adsorption and desorption phases of water vapor exposure and found that while the desorption data was reproducible over multiple exposures, the adsorption data for exposures two and beyond failed to reproduce the data from the first exposure. For the subsequent adsorption exposures, increased water uptake was measured compared to exposure one, but no trend was found between the amount of water uptake and exposure number (Mooney et al. 1952). The authors hypothesized that simply reducing the vapor pressure of water above a sample during the desorption phase was not adequate to completely dry the montmorillonite sample to the same degree as the original sample and thus subsequent cycles experienced additional water activity during adsorption due to the presence of retained interlayer water (Mooney et al. 1952, Kijne 1969).

Our goal in this work is to improve the understanding of how the generation method, sample preparation, and chemical composition of mineral dust aerosol impacts light interaction as a function of relative humidity. To do so we measure the extinction based optical enhancement resulting from humidity increases, fRH_{ext}, for montmorillonite aerosol using cavity ring-down spectroscopy (CRD) at 532 nm in controlled laboratory experiments. Aerosol are dry generated, and separately wet generated and dried from suspensions of six different concentrations to investigate the generation method. Further, montmorillonite powder dried and reclaimed from suspension was dry generated to investigate the role of wet processing. We also measure fRH_{ext} via dry generation for two types of natural montmorillonite, a Ca^{2+} rich sample from Texas and a Na^{+} rich sample from Wyoming, to investigate the effect of interlayer cations. In all cases, calculations were used to compare optically measured fRH_{ext} data to previous literature by conversion to the physical growth factor. Finally, the impact on remote sensing by atmospheric processing caused by variable water content conditions likely experienced by ambient montmorillonite particles during transport is discussed.

3.3 EXPERIMENTAL

Clay aerosol were prepared from Ca-montmorillonite (The Clay Minerals Society, STx-1b) and Na-montmorillonite (The Clay Minerals Society, SWy-2). Aerosol samples were generated through both wet and dry methods. Wet samples of Ca-montmorillonite were prepared by adding the dry clay to HPLC grade water (Fisher Chemical) in 1 %, 5 %, 10 %, 15 %, 20 %, or 30 % (w/w) suspensions. For the remainder of the chapter we define the weight percent as the amount of clay instead of the amount of water in suspension as used in the introduction to

describe the work of Svensson and Hansen (2013). Each individual suspension was placed on a magnetic stir plate to maintain homogeneity as liquid was drawn into the block of a Collison atomizer. Polydisperse aerosol samples are generated using nitrogen gas (N_2, Airgas), flowing at 4 L/min, forced through a small orifice to nebulize the suspension. The aerosol sample was then dried using silica gel beads housed inside of a diffusion dryer (~15 L) achieving a low relative humidity, RH < 10 %. The flow continued through the instrument path as depicted by Figure 3.1 and described below.

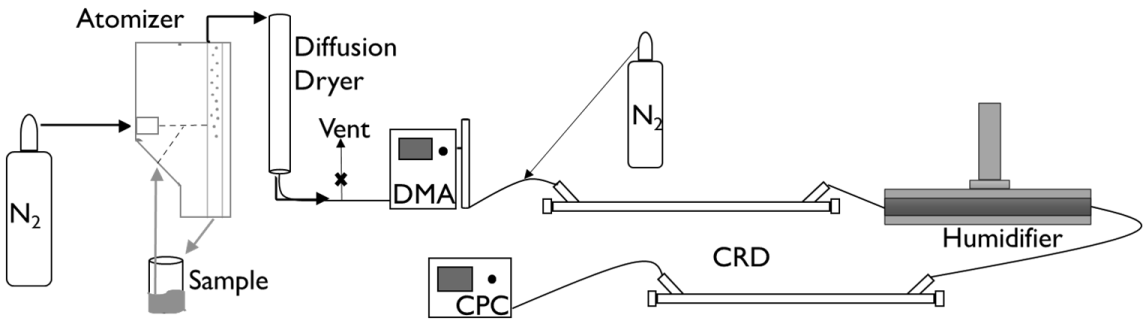

Figure 3.1. Experimental design for optical measurements of montmorillonite extinction as a function of RH with wet generation. DMA – differential mobility analyzer, CPC – condensation particle counter, and CRD – cavity ring-down spectrometer.

Dry samples, of both Ca-montmorillonite and Na-montmorillonite, were generated using a side arm flask attached to a wrist action shaker (Burrell, model 75) as depicted in Figure 3.2 (Morang et al. 2018). The flask contained 2.0 g of the dry montmorillonite powder along with four Teflon coated stir bars. Through the top of the flask, 1.0 L/min of N_2 gas was introduced as a carrier gas. The flask was agitated for the duration of the experiment causing dust to be entrained in the N_2. The clay aerosol sample then traveled vertically up through a ~15 L glass settling volume with a diameter of ~15 cm which allowed the largest generated particles to settle by gravity. After the settling volume the particles passed through stages 3 and 2 of a cascade impactor (PIXE

International Corporation, model I-1) removing particles larger than 1000 and 500 nm, respectively.

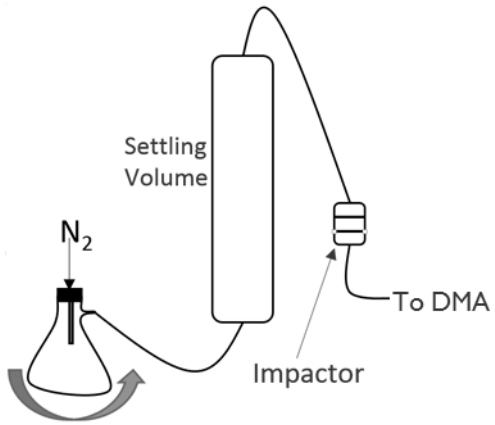

Figure 3.2. Experimental design for dry generation. N_2 flowed through an agitated side arm flask to entrain aerosol in the gas flow. The aerosol then passed through the glass settling volume and a PIXE impactor to minimize large particles entering the DMA. Subsequent optical measurements of extinction as a function of RH are completed as depicted in Figure 3.1 from the vent followed by the DMA.

In addition to dry generating the Ca-montmorillonite as received, experiments were performed to dry generate samples from reclaimed montmorillonite powder. Briefly, a 10 % (w/w) suspension of the clay in water was first vacuum filtered in a Büchner funnel. The still wet clay was scraped from the filter paper with a metal spatula and placed in an open glass jar inside a desiccator containing $CaSO_4$ (W.A. Hammond Drierite^{TM} Company Ltd., 7778-18-9) for two days until it appeared dry, resembling a dry, cracked lakebed. This montmorillonite was then transferred to a mortar and pestle to break up large pieces followed by one additional day of drying in the desiccator at which point the sample resembled the original clay. The resulting reclaimed clay was then dry generated as described above and depicted in Figure 3.2.

In both wet and dry generation experiments, conductive tubing (¼" ID) was used to connect each portion of the setup, limiting the length to minimize particle loss. Following generation, the

aerosol flow continued past a vent as depicted by Figure 3.1. This vent sent a portion of the flow needed for generation to a waste hood so the aerosol flow rate through the differential mobility analyzer (DMA, TSI 3081L) was 0.75 L/min. The DMA was operated at the recommended 10:1 ratio of sheath flow to aerosol flow. For the work presented here, particles were selected at a mobility diameter D_m = 200 nm, where doublets were not measured but may contribute to the measured extinction. Doublets were minimized for wet generation by choosing D_m larger than the mode diameter of the distribution (~100 nm) as determined by a scanning mobility particle sizer (SMPS, TSI 3936). For dry generation, doublets were minimized using the settling volume and PIXE impactor prior to the DMA. Further, because fRH_{ext} is a ratio of extinction between the two cavities of the CRD, the impact of the doublets was minimized. In order to achieve the required 1.5 L/min flow rate for the condensation particle counter (CPC, TSI 3775), ~0.75 L/min of particle free N_2 was added between the DMA and the CRD used for extinction measurements at a wavelength of 532 nm. The CRD used in these experiments has been described previously (Baynard et al. 2007, Garland et al. 2007, Lack et al. 2009, Attwood and Greenslade 2011).

Briefly, CRD consists of five main components: the laser source (Nd:YAG, Quantel USA), a series of optics (Thor Labs), the sample cavities (custom), the photomultiplier tube detector (Hamamatusu H9433-03MOD), and a computer interface to digitize the data (NI-USB-6259 BNC). Within the optical cavity, a light pulse is reflected multiple times between highly reflective mirrors (Advanced Thin Films) on the ends of the cavity. On each pass a small amount of light is transmitted through the mirrors allowing for the detection system to monitor the exponential decay of intensity with time (Herbelin et al. 1980, O'Keefe and Deacon 1988, Wheeler et al. 1998).

For these experiments the CRD consisted of two cavities to measure aerosol extinction. Between the two cavities, a custom permeable membrane (Microdyn Technologies Inc.) humidifier was used to control the RH in the second cavity by ramping temperature with heating tape (Watlow, 1015C 06). RH of the aerosol flow was ramped at ~1.5 %/min by changing the set point of the heater (Watlow, PM6C1KK-AAAAAAA) controlling the tape by 5 °C every 15 minutes until trial termination when the raw RH reading was ~93 %. The raw values were subsequently adjusted using a calibration curve obtained by measuring the RH over three saturated salt solutions (LiCl, NaCl, and K_2SO_4) with known RH values (11, 75, and 97 % RH, respectively). During the RH ramping period, the extinction coefficient, σ_{ext} (cm^{-1}), was continuously measured in both cavities as the aerosol sample passed through the system. The flow terminated at the CPC where particle concentration, N, was measured as a function of time. The extinction cross section, C_{ext}, was then calculated separately for each cavity using Equation (3.1). Average C_{ext} values were calculated from 80 s of optical measurements corresponding to ~1500 laser shots.

$$C_{ext} = \frac{\sigma_{ext}}{N} \tag{3.1}$$

The particle concentration in each cavity was corrected for the nitrogen purge flow present in the CRD. For these experiments, the high flow (1.5 L/min) through the CRD helped to minimize the purge dilution to ~2 and 6 % of the total flow, making this correction small in comparison to C_{ext}. The dilution was different between the two cavities since purge flow was introduced in front of each of the four highly reflective mirrors resulting in increased dilution as the aerosol passed through the system. fRH_{ext} was then calculated with Equation (3.2) and reported as a function of RH.

$$fRH_{ext}(RH) = \frac{C_{ext}(RH)}{C_{ext}(Dry)} \tag{3.2}$$

To better compare with previous literature, two methods of interpreting the fRH_{ext} were utilized. The first exploits an exponential relationship between fRH_{ext} and RH to generate a curve fit to measured data, thus allowing extrapolation or interpolation to RH values not experimentally measured (Kotchenruther et al. 1999). The second is based on Mie theory and converts optically measured fRH_{ext} to the physical growth factor (GF) (Garland et al. 2007).

A recent review article considered many relationships between fRH_{ext} and RH showing nine equations had very good agreement to measured data for non-deliquescing aerosol (Titos et al. 2016). The authors suggested using any of the two parameter fits, such as Equation (3.3) where a and b are fit coefficients, since they are easy to apply and agree well with steady growth fRH_{ext} measurements (Kotchenruther et al. 1999, Titos et al. 2016). Equation (3.3) was fit to measured fRH_{ext} data using a χ^2 minimization routine within Igor Pro.

$$fRH_{ext} = 1 + a\left(\frac{\%\,RH}{100}\right)^b \tag{3.3}$$

Calculating the physical growth factor from the measured fRH_{ext} allows for an expanded comparison to previous literature. GF is a ratio of the humidified particle diameter to the dry particle diameter and is reported based on observed physical size changes. In this model, Mie Theory is used to calculate the diameter of the humidified particles with the known CRI of the two components, water and montmorillonite, in correct ratios (Egan and Hilgeman 1979, Bohren

and Huffman 1983). Previous studies have further explained the calculations within the model (Garland et al. 2007, Attwood and Greenslade 2011).

3.4 RESULTS AND DISCUSSION

To examine the impact of water in the generation process contributing to experimental differences, the measured fRH_{ext} at two different RH values, 85 and 94 %, for STx-1b, Ca-montmorillonite, as a function of clay weight percent is shown by the left y-axis in Figure 3.3. These relative humidity values were selected as a standard value and the highest measured value; further, they show significant changes. For the x-axis, the points at 100 % (w/w) correspond to dry generated aerosol and the rest were wet generated from a suspension of the clay weight percent. At both RH values there is a clear dependence of fRH_{ext} on the amount of clay in the suspension used for wet generation. Starting at low clay concentration and up to 15 % (w/w), fRH_{ext}(94 %) is fairly constant with measured values ~2.6 corresponding to substantial extinction increase by the particles. Over the same weight percent range, fRH_{ext}(85 %) is similarly constant with a value of ~1.7 representing less extinction enhancement than at 94 % RH, as expected. Above 15 % (w/w), there is a sharp decrease in fRH_{ext} for both 94 and 85 % RH. At 30 % (w/w), fRH_{ext} of 1.49(7) and 1.24(5) agree, within uncertainty, to dry generation aerosol measured values, represented by 100 % (w/w), of 1.39(4) and 1.22(4) for 94 and 85 % RH, respectively.

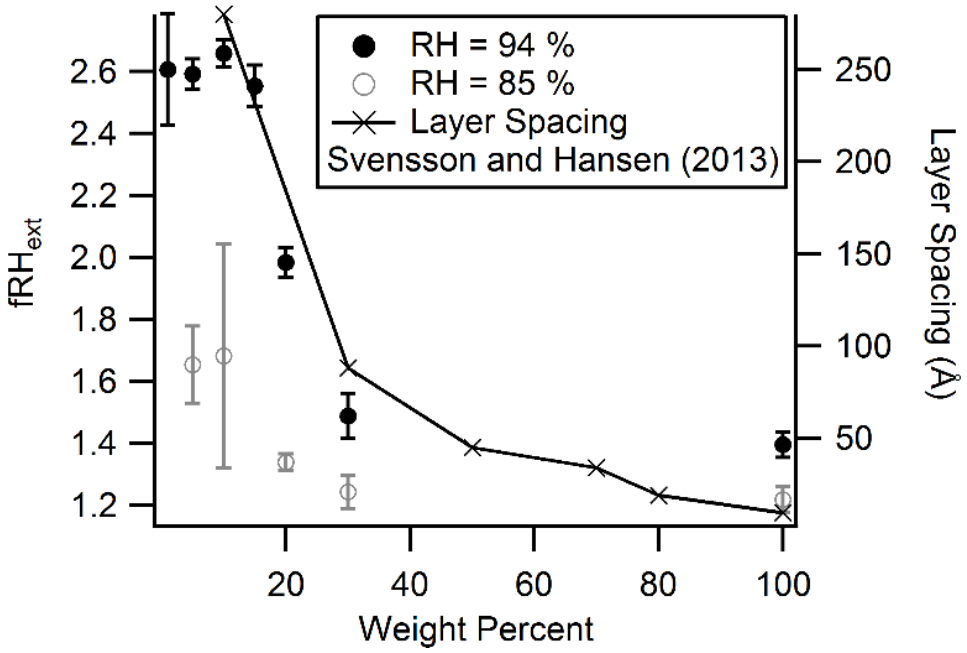

Figure 3.3. Left y-axis: fRH$_{ext}$ as a function of weight percent of Ca-montmorillonite (STx-1b) suspension used for aerosol generation. The points at 100 weight percent are dry generated while the rest are wet generated. The filled black circles represent measured values at 94 % RH and the open grey circles represent 85 % RH. Error bars on each point represent the standard deviation of at least three replicate trials. Right y-axis: XRD measured aluminosilicate layer spacing for Na-montmorillonite suspended in water by Svensson and Hansen (2013). The measurements are represented by crossed points connected by a line to help guide the eye.

The observed trends indicate that differences between measured fRH$_{ext}$ for aerosol wet generated from low weight percent suspensions and dry generation is related to the initial water present in the particles exiting the DMA (Mooney et al. 1952, Kijne 1969). Those authors measured increased water uptake for montmorillonite samples that were not completely dried. For our wet generation samples, the amount of water present in a particle after the DMA is related to the atomization process and the effectiveness of the diffusion dryer. We have no direct observation of particle water content for aerosolized particles, however, we can consider the XRD measured layer spacing of homoionic Na-montmorillonite suspensions as a function of the clay weight percentage, reported previously and shown by the right y-axis in Figure 3.3, to be representative of the water content of the particles generated from our suspensions (Svensson and Hansen

2013). Similar to our results, the authors measured a large, sharp increase in layer spacing distance between 10 and 30 % (w/w) montmorillonite. For this reason, we hypothesize that wet generation produces particles with variable water content depending on the concentration of the suspension used for atomization.

Variable amounts of water in suspension could be correlated with water content of the aerosol particles since all wet generation samples are dried for the same amount of time at room temperature. Within the dryer, water is removed from the particles primarily by evaporation as the RH of the carrier gas is reduced through removal of water vapor by the silica gel beads. In this evaporation regime, interlayer water is difficult to remove from the particles due to the negative value of Gibbs free energy for cation hydration, and therefore is a non-spontaneous process (Kijne 1969). At low clay weight percent there is a large amount of interlayer water, approaching saturation, resulting in measured fRH_{ext} reaching a stable value. Our diffusion dryer can effectively remove some portion of the excess water since the energetics of hydration become minimized with added water. Similarly, Mooney et al. (1952) posited that water vapor desorption measurements are reproducible as long as the sample reaches a threshold amount of water in the structure. It is likely interlayer water that is not dried from the particles contributes to the difference in measured fRH_{ext} as a function of suspension concentration since increased interlayer water would yield increased water uptake and thus greater fRH_{ext}.

Greater enhancement to fRH_{ext} for wet generation compared to dry could be explained by changes in cation distribution or surface area availability for the wet generated particles resulting from processing while in suspension (Stul and Vanleemput 1982, Stul and Vanleemput 1982,

Garimella et al. 2014). We investigated the possible effects of processing in suspension for wet generated particles by reclaiming clay from suspension and dry generating the resulting powder. To compare cases, measured fRH_{ext} as a function of RH is shown in Figure 3.4 for three STx-1b montmorillonite aerosol samples: one wet generated from 10 % (w/w) suspension, one dry generated from clay reclaimed from a 10 % (w/w) suspension, and one dry generated from the bulk powder. All three aerosol samples show little extinction enhancement up to 60 % RH with $fRH_{ext}(60\ \%) \approx 1$. The clay aerosol extinction begins to increase steadily, at similar rates, between 60 and 75 % RH. Above 75 % RH, the 10 % (w/w) wet generated aerosol shows increased extinction compared to the dry generation methods, with $fRH_{ext}(94\ \%) = 2.66(5)$. The dry generation data sets show good agreement with each other, within the calculated uncertainties, continuing extinction enhancement to the maximum RH studied. For fresh dry generated $fRH_{ext}(94\ \%)$ is 1.39(4) and for reclaimed dry generated the extrapolated value is 1.43(3). The extrapolated value is calculated with Equation (3.3), using the fit coefficients determined from the entire range of measured data found in Table A2 in the Appendix.

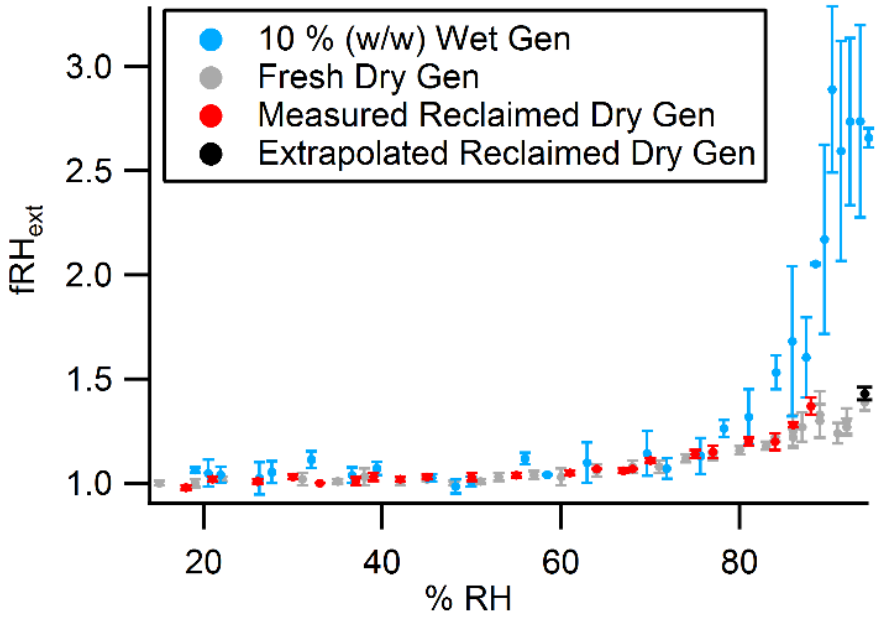

Figure 3.4. fRH_{ext} as a function of RH for Ca-montmorillonite (STx-1b) aerosol generated with different methods. The filled aqua circles represent wet generated 10 % (w/w) suspension of clay in water, the filled grey circles represent dry generated fresh powder, the filled red circles represent measured dry generated reclaimed powder which had previously been mixed in a 10 % (w/w) suspension, and the filled black circle represents Equation (3.3) extrapolated reclaimed dry generated. The error bars on each data set represent the standard deviation of at least three replicate trials.

The similarity between the two dry generation samples suggests no irreversible change occurs to the montmorillonite in suspension. Even with this observation, there is still the possibility that due to differences in the drying mechanism between the reclaimed montmorillonite powder and the wet generated particles, ion redistribution could occur in the wet generated case. If more ions were present on the surface of the aerosol sample, instead of within the interlayer space, it might behave more like a mixed aerosol of mineral and salt which would be more hygroscopic than the parent clay, depending on the ion concentrations. Since there is little change between the two dry generated samples, the amount of redistributed ions is presumed to be small, and based on other literature this would minimize the impact on water activity and thus fRH_{ext} (Attwood and Greenslade 2012, Garimella et al. 2014). Attwood and Greenslade (2012) measured fRH_{ext} for aerosol wet generated from 10 % (w/w) montmorillonite suspensions mixed with a range of

NaCl concentrations. In the study, fRH_{ext}(90 %) increased as a function of the NaCl concentration, with a factor of approximately two enhancement for a 0.1 % (w/w) NaCl and 10 % (w/w) montmorillonite compared to pure montmorillonite. Garimella et al. (2014) measured the concentrations of extracted ions from a filtered montmorillonite suspension with at least an order of magnitude lower concentration than the salt in suspension used by Attwood and Greenslade (2012) and therefore we would expect less than a factor of two enhancement between fresh dry generated and 10 % (w/w) wet generation if redistribution was the only explanation. Yet, we measured a factor of approximately two enhancement to fRH_{ext}(90 %) between fresh dry generated and 10 % (w/w) wet generated samples leading to the conclusion that other factors contribute to the observed enhancement.

Another possible cause for the difference between wet and dry generated optical enhancement is that suspending montmorillonite causes the clay particles to restructure into different layer orientations from those in the bulk powder resulting in changes to surface area (Stul and Vanleemput 1982, Brindly and Brown 1984). Since the measured fRH_{ext} for the two dry generation cases agree within uncertainty, this suggests there is little difference between the powders. BET quantification of surface area would be a useful future experiment to determine whether aggregation during drying impacts the surface area, however, it is limited because the N_2 adsorption gas used by the instrument is only able to access the outer surface of montmorillonite and may miss important internal structures (Norrish et al. 1954, Cases et al. 1992).

To provide additional context for our results, the GF, which for an aerosol component is an intensive parameter (not dependent on size or number of particles), allows for broader

comparison to previous literature where size may not have been controlled. Previously reported measurements of the GF for montmorillonite are compared to select values calculated from our experimental results, using the fRH_{ext} conversion model, in Table 3.1 (Mooney et al. 1952, Cases et al. 1992, Xu et al. 2000, Schuttlefield et al. 2007, Hatch et al. 2012). Most literature values are larger than the GF calculated in this work, though in some comparisons the uncertainties overlap.

Table 3.1. Growth factor for montmorillonite at 68 and 85 % RH for various literature studies.

Reference:	GF at 68 % RH	GF at 85 % RH	Comments:
Mooney et al. 1952	1.12(4)	1.14(5)	Bulk - adsorption gravimetry Wyoming Na-montmorillonite Water suspension vacuum/heat dried
Cases et al. 1992	1.09(4)	1.14(5)	Bulk - microbalance Wyoming Na-montmorillonite Water suspension heat dried
Xu et al. 2000	1.12(2)	1.19(4)	Thin film - microbalance SWy-1 Na-montmorillonite 0.25 % (w/w) suspension air dried
Schuttlefield et al. 2007	1.10(1)	1.11(2)	Bulk - quartz crystal microbalance Alfa Aesar montmorillonite Water suspension air dried
	1.14(1)	-	Bulk - quartz crystal microbalance SWy-2 Na-montmorillonite Water suspension air dried
	1.37(1)	-	Bulk - quartz crystal microbalance SAz-1 Mg-montmorillonite Water suspension air dried
Hatch et al. 2012	1.14(1)	-	Bulk - ATR-FTIR SWy-2 Na-montmorillonite 0.0003 % (w/w) suspension N_2 dried
This work	1.05(1)	1.17(4)	Aerosol - CRD STx-1b Ca-montmorillonite 10 % (w/w) wet generated
	1.03(1)	1.07(2)	Aerosol - CRD STx-1b Ca-montmorillonite Fresh dry generated
	1.04(1)	1.13(2)	Aerosol - CRD SWy-2 Na-montmorillonite Fresh dry generated

Our estimated GF may differ from prior results for various reasons including: the type of montmorillonite used, measurement sensitivity, and/or fRH_{ext} conversion model limitations which will be examined below. Previous literature has indicated that cations play a crucial role in clay water activity by assisting in the molecular arrangement of adsorbed water (Norrish 1954, Kijne 1969, Brindly and Brown 1984, Hsiao and Hedström 2017). In one study, increased water uptake was predicted from Ca-montmorillonite to Na-montmorillonite to Mg-montmorillonite, where Mg-montmorillonite has the most water uptake (Norrish 1954). The authors based their predictions on an index value, calculated for each cation by considering the charge of the cation and its hydration energy. In that study, samples of montmorillonite were assumed to be homoionic, whereas natural samples contain a mixture of cations, so direct comparison to the results in Table 3.1 is not possible but the trend can be useful. To investigate the cation effect on dry generated aerosol fRH_{ext} measurements, we compare Texas (STx) sourced montmorillonite richer in Ca^{2+} cations to Wyoming (SWy) sourced montmorillonite containing additional Na^{+}. At 68 % RH, the GF values of 1.03(1) and 1.04(1), for STx and SWy respectively, agree for the two varieties of montmorillonite. Much like with the results presented in Figure 3.4, montmorillonite samples generally have similar water activity at this RH with little uptake as further demonstrated by the overlap with our wet generation GF of 1.05(1). At 85 % RH, the GF for SWy (Na^{+} rich) of 1.13(2) is larger than the GF for STx (Ca^{2+} rich) of 1.07(2). Our samples show a similar trend to Norrish et al. (1954) with Na-montmorillonite swelling more than Ca-montmorillonite. Most of the literature results used varieties of SWy clays, which we compare to below, with some Arizona (SAz) sourced montmorillonite containing additional Mg^{2+}, and the Alfa Aesar montmorillonite with unknown cation concentrations. SAz

montmorillonite had the highest measured GF at 68 % RH which further agrees with the trend determined by Norrish (1954).

To examine the measurement sensitivity and model limitations, we compare our SWy montmorillonite dry generation results to other Wyoming sourced samples presented in Table 3.1. At 68 % RH our value of 1.04(1) is low compared to the GF of other SWy samples with overlap of uncertainties to the Cases et al. (1992) value of 1.09(4). When there is a small amount of water associated with the sample, such as at 68 % RH, the sensitivity of the measurement is important. For the mass based approaches shown in Table 3.1 the sensitivity of the balances are at least an order of magnitude lower than the measured mass change allowing for a robust measurement with a significant difference. For example, Xu et al. (2000) used a balance with 1 μg sensitivity to measure a water mass deposition of 1.8 mg onto a 10 mg film of montmorillonite, corresponding to the calculated GF of 1.12(1). Contrast this with GF calculated from fRH_{ext} based on CRD extinction measurements where at 68 % RH, the measured extinction values are not statistically different. The humidified extinction ($8.3(5) \times 10^{-8}$ cm^{-1}) agrees within the uncertainty to the dry extinction ($7.5(5) \times 10^{-8}$ cm^{-1}).

Further, at 68 % RH we approach the fRH_{ext} conversion model limitations. Consider adsorbing water onto the rough surface of a montmorillonite particle. At the beginning there is little change to the particle diameter (200 nm) from adsorption since water is first deposited on the surface, filling voids and depressions before a complete monolayer forms (Cases et al. 1992). After surface coverage, water begins to penetrate unevenly into the interlamellar space (Cases et al. 1992). In this proposed coverage model the particle size experiences little change since a

monolayer of water is only ~2.8 Å. Depending on the exact distribution of water on the particle we may also consider that the homogeneous mixing assumed in our model may not be appropriate. Early stages of adsorption are better represented by a core shell model, though changing the mixing assumption results in a calculated GF at 68 % RH for dry generated SWy of 1.03(1) which agrees within uncertainty to the homogeneously mixed value. Since our dry and humidified extinction measurements are equivalent within the error and the model selection is not sensitive to small water content, this likely explains why our calculated GF values at 68 % RH do not better match other literature.

At 85 % RH, when more water is present, our calculated GF for dry generated SWy (Na rich) of 1.13(2) agrees with most of the other values within the calculated uncertainties. The amount of water adsorbed by montmorillonite is now enough to form at least bilayer surface coverage as well as hydrate the cations (Cases et al. 1992). The fRH_{ext} calculated GF of 1.13(2) represents particle growth to 225 nm compared to the initial 200 nm dry generated particle corresponding to extinction enhancement of 40 % and exceeding the uncertainties on the extinction measurements. Given the small size of a water bilayer (5.6 Å) compared to our calculated growth (25 nm), we predict substantial amounts of water penetrate into the layers. This morphology may now be better represented by the homogeneous mixing assumed in our model resulting in calculated values within agreement to literature. Additionally, while the model is not the best representation of the shape of the clay particles, previous literature has shown that since global climate models are often built assuming spherical particles, the input data should be derived with a similar level of theory otherwise model errors will compound and increase overall uncertainty in climate predictions (Saleh et al. 2016). Future refinements to the model will include incorporating a

newly derived refractive index assuming spherical morphology for irregularly shaped montmorillonite aerosol instead of the bulk value (Morang et al. 2018).

The results of this chapter have implications related to determining atmospheric cloud condensation nuclei (CCN) concentration. Commonly, CCN concentrations are calculated by the relationship to satellite measured aerosol optical depth (AOD) through the use of various parameterizations (Liu and Li 2014, Shinozuka et al. 2015). AOD is defined as the total extinction for a column of air between the satellite and the surface of the Earth and is a function of the number of particles present and the associated optical properties of the particles (Ma et al. 2013). Measured column extinction at visible wavelengths is normally dominated by large particles, such as mineral dust, even though these particles contribute little to the number concentration due to the contribution to total aerosol volume and large extinction cross sections (Waggoner et al. 1981, Seinfeld and Pandis 2006). AOD is inverted to the particle size distribution with various assumptions built in to the model including the refractive index (Zhang et al. 2017). For the swellable clays, such as montmorillonite, extinction increases and the refractive index changes as a function of RH without changing the number concentration. In this way, even though clay aerosols contribute very little to CCN concentration (typically particles between 50-120 nm), the relationship between extinction and CCN concentration as a function of RH (especially > 75 % RH) has been shown to contribute uncertainty in remote sensing and as such researchers commonly exclude dust dominated days from analysis (Levy et al. 2013, Liu and Li 2014, Shinozuka et al. 2015).

The relationship between extinction and CCN concentrations is further complicated in the presence of montmorillonite aerosol based on the results of this chapter, and work by others, showing that water uptake is affected by the initial presence of water (Mooney et al. 1952, Sorjamaa and Laaksonen 2007, Kumar et al. 2011). In this case fRH_{ext} is likely a function of ageing such that the dry generated results from this work represent fresh aerosol activity and the low concentration wet generated suspensions represent transported dust. As dust is transported through the atmosphere, cycling through regions of high and low humidity, it is unlikely the particles will ever be dried to the same degree as in arid source region.

In conclusion, in this chapter we have measured extinction enhancement for montmorillonite aerosol as a function of relative humidity. Our data indicates that the concentration of the suspension used for wet generated Ca^{2+} rich montmorillonite samples influences measured fRH_{ext} by producing particles with variable amounts of initial water where increased initial water leads to increased water uptake. Further, we observed that dry generated samples, both unprocessed and reclaimed from water suspension, have similar measured water uptake which indicates the possibility of drying wet generated aerosols. In this regard, future studies could be used to confirm the presence of water within the particles; these studies could include implementing a heated dryer tube to facilitate water evaporation before optical interrogation or the use of microscopy, such as SEM or TEM, imaging the generated particles under high vacuum conditions to quantify potential diameter change such as in work by Dinneen et al. (2017).

Additionally, future studies should investigate parameters which may affect the sharp transition in fRH_{ext} as a function of suspension concentration shown in Figure 3.3 including studying wet

generated samples with similar drying mechanisms to this work but with homoionic clays. The water/cation interaction is fundamental to clay swelling which suggests that particle drying may also be dependent on the energetics involved in the hydration process. Preparation of a completely dry particle is related to the amount of initial water present and the effectiveness of the diffusion dryer. Cation choice will potentially effect both of these, resulting in a shift along the x-axis for the steep transition portion of the data depending on the interlayer cation present. In terms of the GF calculations conducted with the fRH_{ext} conversion model we showed that at high RH the model produced results within the range of previous literature. At lower RH the model calculates low values of GF compared to literature, possibly due to the small change in diameter and refractive index, and therefore measured extinction, at the initial stages of water adsorption.

Finally, our results indicate that atmospheric processing may result in variable behavior in terms of water uptake, and thus particle extinction, for aged montmorillonite particles compared to freshly emitted. Based on our results, particles will contain more water after transport than at an arid source region resulting in enhanced subsequent water uptake. The enhanced water uptake would contribute additional uncertainty in applying remote sensing to determine ambient particle concentrations within dust dominated aerosol plumes. In the future, we will probe these ageing dynamics by performing experiments with multiple dry and humidify steps.

CHAPTER 4

CONCLUDING REMARKS

Atmospheric aerosol alter the Earth's climate by interacting with solar radiation by scattering and absorbing. The cumulative result of aerosol particle light interactions remains to be fully quantified. Several reasons for this are: unknown or limited knowledge of wavelength dependent complex refractive index (CRI) for all aerosol components, an incomplete understanding of water activity on particles, and the lack of a set of computational models capable of reproducing both laboratory and field based experimental results.

The custom-built Aerosol Extinction Differential Optical Absorption Spectrometer (AE-DOAS) was used to measure light extinction of laboratory generated aerosol to obtain the wavelength dependent CRI from visible wavelengths into the UV. In Chapter 3 monodisperse polystyrene latex spheres (PSL) were wet generated from water suspension. The retrieved real portion (n) of the CRI agreed with previous literature and/or other measurement techniques when wavelength overlap existed with results detailed directly below. Further, the retrieved imaginary portion (k) of the CRI is then discussed.

For PSL, using an iterative computational error minimization routine between experimental results and Mie Theory model, the retrieved n agrees with previous results down to $\lambda = 360$ nm

for aerosol derived results and down to 235 nm compared to thin film derived results. When the Cauchy model is used to represent measured n, results are only valid over small wavelength ranges. Previously derived Cauchy model coefficients by Ma et al. (2003) for PSL failed to reproduce the measured results here in the UV. Other models, such as Sellmeier formula, were considered, but failed to improve agreement over wide wavelength ranges. The lack of a sufficient model to represent the wavelength dependence of the real part of the refractive index demonstrates the need to continue to use instruments like the AE-DOAS. Further analysis of the results showed that more precise n can be retrieved by carefully choosing the particle diameters. Extending the AE-DOAS capabilities to retrieve n at the smallest wavelengths, where a good detection limit exists ($\lambda \sim 235$ nm), will require small particles sizes as these are most sensitive to change in n when considering extinction efficiency versus size parameter representations used for retrievals at specific wavelengths. This is possible for PSL, since the initial suspension used to wet generate the aerosol contains a nearly monodisperse sphere size. However, caution is needed when selecting small particle sizes for other aerosol components.

We show that exclusively measuring extinction to derive n, for a specific type of aerosol, produced comparable results to previous literature and other measurement techniques. Deriving the imaginary portion of the CRI is more complicated than obtaining n. The imaginary portion is related to absorption and for most aerosol components absorption is negligible compared to scattering. Chapter 2 emphasizes the need for *in situ* absorption measurements since the retrieved k for PSL aerosol has large error bars and is different from the k determined from measured absorption by thin films. In this case, bulk materials such as thin films may not reproduce the

structural characteristics of particles. Additionally, the polymer formulation may not have been replicated between the experiments.

In Chapter 3, the optical enhancement (fRH_{ext}) was measured for aerosol composed of the clay mineral montmorillonite using a cavity ring-down (CRD) spectrometer. Wet generation from suspensions of montmorillonite and dry generation from the fresh powder were compared. Results demonstrated elevated fRH_{ext} for wet generated aerosol from suspensions with low concentrations (< 15 % (w/w)) when compared to higher suspension concentrations and dry generated particles. First, the results demonstrated that careful consideration should be taken when generating aerosol in the laboratory to recreate natural processes. Second, the results have atmospheric transport implications, such as the need to better understand the dynamics of water uptake for *in situ* particles. As a particle is transported through the atmosphere it will encounter regions of low and high humidity such that the fRH_{ext} at the source may be significantly different from the fRH_{ext} following transport. Future controlled laboratory experiments should focus on probing the dynamics of water interaction by varying the type of interlayer cation within the montmorillonite lattice or implementing a more aggressive heated drying approach.

The previous sections have discussed the results, implications, and future directions for acquiring physical properties of aerosol. However, even if all physical properties of aerosol were known there remains challenges implementing these properties into models such that they will correctly reproduce experimental results. Mie Theory was used in both chapters since this theory is readily available and is commonly used. However, Chapter 3 would benefit from a model which accounts for deviations from solid, homogeneous, and spherical particles such as an improved

T-matrix theory. In all chapters the generated particles were assumed to be single component whereas ambient particles are almost always a mixture of multiple components. Calculating the CRI for a mixture could be improved by knowing the exact mixing state of the components in a particle. Even for a spherical particle with known composition, calculating the refractive index for a composite particle from the components is still challenging. Some morphologies, such as core shell, with available models would be easier to use than randomly distributed compositions.

In conclusion, both the AE-DOAS and CRD have been used to measure aerosol optical properties, including quantifying extinction directly and deriving refractive index in the visible region of the spectrum. Some results have extended into UV wavelengths and future experiments would benefit from method refinement described here to improve sensitivity. Further, laboratory produced aerosol should be generated by techniques which most closely mimic natural processes so that results can be used to interpret satellite and other field data. These experiments have provided results for specific aerosol processing cases, and future experiments should target additional relevant experimental conditions which will aid in understanding the dynamics of atmospheric ageing during transport. Finally, an important overarching conclusion is that even in the laboratory experimental control is difficult. Many variables exist including size, shape, and chemical composition which can be changed between experiments and different from particle to particle. These experiments have shown that often balance must be sought in selecting experimental design. Challenges are even greater in the field where particles are less controlled.

APPENDIX

Table A1. Numerical complex refractive index retrieved values for polystyrene latex spheres. Values are presented graphically in Figures 2.3 and 2.4 in Chapter 2.

λ (nm)	n	Δn	k	Δk
221	2.2	0.5	0	6
222	2.2	0.3	0.3	0.4
224	2.10	0.17	0.2	0.3
226	2.03	0.08	0.08	0.11
228	2.00	0.04	0.04	0.05
231	1.942	0.001	0.000	0.001
233	1.960	0.002	0.000	0.05
235	1.92	0.07	0.03	0.05
236	1.91	0.04	0.02	0.03
238	1.90	0.03	0.02	0.03
240	1.878	0.003	0.000	0.002
242	1.849	0.004	0.000	0.017
245	1.862	0.005	0.000	0.004
247	1.880	0.001	0.002	0.003
249	1.900	0.003	0.001	0.002
250	1.80	0.01	0.00	0.08
253	1.816	0.004	0.000	0.005
254	1.831	0.003	0.000	0.002
256	1.796	0.017	0.01	0.03
258	1.696	0.006	0.005	0.006
260	1.711	0.006	0.005	0.006
263	1.726	0.007	0.005	0.005
265	1.740	0.009	0.005	0.005
267	1.76	0.01	0.005	0.011
269	1.770	0.013	0.00	0.02
271	1.76	0.03	0.05	0.03
272	1.75	0.03	0.06	0.03
275	1.74	0.03	0.06	0.03
276	1.73	0.02	0.06	0.04
279	1.72	0.02	0.06	0.05
280	1.69	0.02	0.05	0.05
283	1.681	0.019	0.05	0.05
284	1.680	0.017	0.03	0.05
286	1.673	0.018	0.02	0.04
288	1.667	0.016	0.01	0.04
290	1.666	0.014	0.01	0.03

292	1.669	0.017	0.005	0.015
294	1.677	0.017	0.005	0.016
296	1.687	0.017	0.005	0.016
299	1.69	0.02	0.005	0.017
301	1.703	0.019	0.005	0.018
303	1.66	0.03	0.03	0.05
305	1.66	0.02	0.02	0.05
307	1.649	0.015	0.01	0.05
309	1.649	0.012	0.01	0.05
311	1.650	0.015	0.01	0.04
313	1.649	0.013	0.01	0.03
315	1.650	0.013	0.01	0.02
317	1.651	0.015	0.01	0.02
319	1.650	0.016	0.01	0.03
321	1.647	0.016	0.01	0.04
322	1.646	0.017	0.01	0.05
324	1.648	0.017	0.01	0.04
326	1.651	0.017	0.01	0.04
328	1.657	0.018	0.01	0.03
330	1.647	0.019	0.01	0.03
332	1.65	0.02	0.005	0.019
335	1.65	0.03	0.004	0.019
336	1.64	0.03	0.000	0.019
339	1.63	0.03	0.002	0.018
340	1.62	0.03	0.00	0.02
343	1.62	0.04	0.01	0.03
344	1.59	0.04	0.01	0.05
347	1.60	0.03	0.01	0.04
348	1.61	0.03	0.01	0.04
351	1.62	0.03	0.01	0.04
352	1.61	0.03	0.01	0.04
355	1.60	0.03	0.01	0.04
357	1.60	0.03	0.01	0.05
358	1.63	0.03	0.01	0.03
361	1.63	0.03	0.01	0.03
362	1.613	0.019	0.01	0.05
365	1.614	0.018	0.01	0.05
366	1.62	0.02	0.01	0.05
369	1.63	0.02	0.01	0.05

370	1.63	0.02	0.01	0.05
373	1.63	0.02	0.01	0.04
375	1.64	0.02	0.01	0.03
376	1.64	0.02	0.01	0.04
379	1.65	0.03	0.01	0.04
380	1.63	0.02	0.01	0.04
383	1.63	0.02	0.01	0.04
384	1.63	0.02	0.01	0.04
387	1.63	0.02	0.01	0.03
388	1.63	0.02	0.01	0.04
390	1.63	0.02	0.01	0.04
393	1.63	0.02	0.01	0.04
394	1.634	0.019	0.01	0.04
397	1.64	0.02	0.01	0.04
398	1.64	0.02	0.01	0.04
401	1.64	0.02	0.01	0.03
403	1.64	0.02	0.01	0.03
404	1.65	0.02	0.01	0.03
407	1.66	0.02	0.01	0.03
408	1.66	0.02	0.01	0.03
411	1.67	0.02	0.01	0.03
413	1.67	0.02	0.01	0.03
414	1.67	0.03	0.00	0.02
417	1.63	0.03	0.01	0.02
418	1.63	0.03	0.01	0.02
421	1.64	0.03	0.01	0.02

Equation (4.4) was fit to data collected for Ca-montmorillonite sets with complete RH coverage resulting in the coefficients shown in Table 4.1. For all samples a good fit was produced as demonstrated by the χ^2/N^2 values less than 0.5 (Kotchenruther et al. 1999, Titos et al. 2016). The χ^2/N^2 ratios allow for comparison of the goodness of fit for the different generation methods used where fresh dry generation has the best fit and 5 % (w/w) wet generated is the poorest.

Table A.2. Fit coefficients determined for Equation (4.4) for Ca-montmorillonite aerosol generated with various methods. χ^2/N^2 values indicate the goodness of fit of the model to the measured data.

Generation Method:	a	Δa	b	Δb	χ^2/N^2
Fresh Dry Generated	0.47	0.04	4.8	0.4	0.017
Reclaimed Dry Generated	0.58	0.04	4.8	0.3	0.069
5 % (w/w) Wet Generated	1.94	0.06	7.51	0.16	0.478
10 % (w/w) Wet Generated	3.07	0.15	9.3	0.4	0.097
20 % (w/w) Wet Generated	0.75	0.03	4.52	0.17	0.145
30 % (w/w) Wet Generated	0.467	0.014	2.1	0.17	0.040

LIST OF REFRENCES

Aalto, P., K. Hameri, E. Becker, R. Weber, J. Salm, J. M. Makela, C. Hoell, C. D. O'Dowd, H. Karlsson, H. C. Hansson, M. Vakeva, I. K. Koponen, G. Buzorius and M. Kulmala (2001). Physical characterization of aerosol particles during nucleation events. Tellus B. 53:344-358.

Abo Riziq, A., C. Erlick, E. Dinar and Y. Rudich (2007). Optical properties of absorbing and non-absorbing aerosols retrieved by cavity ring down (CRD) spectroscopy. Atmos. Chem. Phys. 7:1523-1536.

Achakulwisut, P., L. Shen and L. J. Mickley (2017). What Controls Springtime Fine Dust Variability in the Western United States? Investigating the 2002-2015 Increase in Fine Dust in the US Southwest. J. Geophys. Res.-Atmos. 122:12449-12467.

Ackerman, T. P. and O. B. Toon (1981). Absorption of Visible Radiation in Atmosphere Containing Mixtures of Absorbing and Nonabsorbing Particles. Appl. Optics 20:3661-3668.

Adler, G., T. Koop, C. Haspel, I. Taraniuk, T. Moise, I. Koren, R. H. Heiblum and Y. Rudich (2013). Formation of highly porous aerosol particles by atmospheric freeze-drying in ice clouds. P. Natl. Acad. Sci. USA 110:20414-20419.

Alexander, J. M., D. M. Bell, D. Imre, P. D. Kleiber, V. H. Grassian and A. Zelenyuk (2016). Measurement of size-dependent dynamic shape factors of quartz particles in two flow regimes. Aerosol Sci. Tech. 50:870-879.

Alfaro, S. C. and L. Gomes (2001). Modeling mineral aerosol production by wind erosion: Emission intensities and aerosol size distributions in source areas. J. Geophys. Res.-Atmos. 106:18075-18084.

Ammann, M., R. A. Cox, J. N. Crowley, M. E. Jenkin, A. Mellouki, M. J. Rossi, J. Troe and T. J. Wallington (2013). Evaluated kinetic and photochemical data for atmospheric chemistry: Volume VI - heterogeneous reactions with liquid substrates. Atmos. Chem. Phys. 13:8045-8228.

Andreae, M. O. and A. Gelencser (2006). Black carbon or brown carbon? The nature of light-absorbing carbonaceous aerosols. Atmos. Chem. Phys. 6:3131-3148.

Angstrom, A. (1929). On the Atmospheric Transmission of Sun Radiation and on Dust in the Air. Geogr. Ann. 11:156-166.

Arnott, W. P., H. Moosmuller, C. F. Rogers, T. F. Jin and R. Bruch (1999). Photoacoustic spectrometer for measuring light absorption by aerosol: instrument description. Atmos. Environ. 33:2845-2852.

Attwood, A. R. and M. E. Greenslade (2011). Optical Properties and Associated Hygroscopicity of Clay Aerosols. Aerosol Sci. Tech. 45:1350-1359.

Attwood, A. R. and M. E. Greenslade (2012). Deliquescence Behavior of Internally Mixed Clay and Salt Aerosols by Optical Extinction Measurements. J. Phys. Chem. A 116:4518-4527.

Baynard, T., E. R. Lovejoy, A. Pettersson, S. S. Brown, D. Lack, H. Osthoff, P. Massoli, S. Ciciora, W. P. Dube and A. R. Ravishankara (2007). Design and application of a pulsed cavity ring-down aerosol extinction spectrometer for field measurements. Aerosol Sci. Tech. 41:447-462.

Bluvshtein, N., J. M. Flores, A. Abo Riziq and Y. Rudich (2012). An Approach for Faster Retrieval of Aerosols' Complex Refractive Index Using Cavity Ring-Down Spectroscopy. Aerosol Sci. Tech. 46:1140-1150.

Bohren, C. and D. Huffman (1983). Absorption and scattering of light by small particles, John Wiley & Sons Inc. Weinheim Germany.

Bond, T. C. and R. W. Bergstrom (2006). Light absorption by carbonaceous particles: An investigative review. Aerosol Sci. Tech. 40:27-67.

Brindly, G. W. and B. Brown (1984). Crystal Structures of Clay Minerals and Their X-Ray Identification, Mineralogical Society. London, UK.

Carrico, C. M., P. Kus, M. J. Rood, P. K. Quinn and T. S. Bates (2003). Mixtures of pollution, dust, sea salt, and volcanic aerosol during ACE-Asia: Radiative properties as a function of relative humidity. J. Geophys. Res.-Atmos. 108.

Cases, J. M., I. Berend, G. Besson, M. Francois, J. P. Uriot, F. Thomas and J. E. Poirier (1992). Mechanism of Adsorption and Desorption of Water Vapor by Homoionic Montmorillonite. 1. The Sodium-Exchanged Form. Langmuir 8:2730-2739.

Charlson, R. J., J. Langner, H. Rodhe, C. B. Leovy and S. G. Warren (1991). Perturbation of the northern hemisphere radiative balance by backscattering from anthropogenic sulfate aerosols. Tellus A 43:152-163.

Charlson, R. J., W. M. Porch, A. P. Waggoner and N. C. Ahlquist (1974). Background aerosol light scattering characteristics: nephelometric observations at Mauna Loa Observatory compared with results at other remote locations. Tellus 26:345-360.

Charlson, R. J., S. E. Schwartz, J. M. Hales, R. D. Cess, J. A. Coakley, J. E. Hansen and D. J. Hofmann (1992). Climate forcing by anthropogenic aerosols. Science 255:423-430.

Chartier, R. T. and M. E. Greenslade (2012). Initial investigation of the wavelength dependence of optical properties measured with a new multi-pass Aerosol Extinction Differential Optical Absorption Spectrometer (AE-DOAS). Atmos. Meas. Tech. 5:709-721.

Chen, Y. and T. C. Bond (2010). Light absorption by organic carbon from wood combustion. Atmos. Chem. Phys. 10:1773-1787.

Chester, R., H. Elderfield, J. J. Griffin, L. R. Johnson and R. C. Padgham (1972). Eolian dust along the eastern margins of the Atlantic Ocean. Mar. Geol. 13:91-105.

Church, J. A. and N. J. White (2011). Sea-Level Rise from the Late 19th to the Early 21st Century. Surv. Geophys. 32:585-602.

DeCarlo, P. F., J. G. Slowik, D. R. Worsnop, P. Davidovits and J. L. Jimenez (2004). Particle morphology and density characterization by combined mobility and aerodynamic diameter measurements. Part 1: Theory. Aerosol Sci. Tech. 38:1185-1205.

Dick, W. D., P. J. Ziemann, P. F. Huang and P. H. McMurry (1998). Optical shape fraction measurements of submicrometre laboratory and atmospheric aerosols. Meas. Sci. Technol. 9:183-196.

Dinar, E., A. Abo Riziq, C. Spindler, C. Erlick, G. Kiss and Y. Rudich (2008). The complex refractive index of atmospheric and model humic-like substances (HULIS) retrieved by a cavity ring down aerosol spectrometer (CRD-AS). Faraday Discuss. 137:279-295.

Dinneen, S. R., M. E. Greenslade and L. F. Deravi (2017). Optical extinction of size-controlled aerosols generated from squid chromatophore pigments. Apl Materials 5.

Dodd, L. E. (1931). Calibration of Abbe refractometer with compensating prisms, to measure refractive index for any wave length. Rev. Sci. Instrum. 2:466-501.

Dutton, E. G., J. J. Deluisi and B. A. Bodhaine (1984). Features of Aerosol Optical Depth Observed at Barrow, March 10-20, 1983. Geophys. Res. Lett. 11:385-388.

Egan, W. G. and T. W. Hilgeman (1979). Optical Properties of Inhomogeneous Materials: Applications to Geology, Astronomy, Chemistry, and Engineering, Academic Press. New York, NY.

Erlick, C., M. Haspel and Y. Rudich (2011). Simultaneous retrieval of the complex refractive indices of the core and shell of coated aerosol particles from extinction measurements using simulated annealing. Appl. Optics 50:4393-4402.

Fissan, H. J., C. Helsper and H. J. Thielen (1983). Determination of Particle-Size Distributions by Means of an Electrostatic Classifier. J. Aerosol Sci. 14:354-357.

Flores, J. M., R. A. Washenfelder, G. Adler, H. J. Lee, L. Segev, J. Laskin, A. Laskin, S. A. Nizkorodov, S. S. Brown and Y. Rudich (2014). Complex refractive indices in the near-ultraviolet spectral region of biogenic secondary organic aerosol aged with ammonia. Phys. Chem. Chem. Phys. 16:10629-10642.

Freedman, M. A., C. A. Hasenkopf, M. R. Beaver and M. A. Tolbert (2009). Optical Properties of Internally Mixed Aerosol Particles Composed of Dicarboxylic Acids and Ammonium Sulfate. J. Phys. Chem. A 113:13584-13592.

French, R. H., K. I. Winey, M. K. Yang and W. M. Qiu (2007). Optical properties and van der Waals-London dispersion interactions of polystyrene determined by vacuum ultraviolet spectroscopy and spectroscopic ellipsometry. Aust. J. Chem. 60:251-263.

Garimella, S., Y. W. Huang, J. S. Seewald and D. J. Cziczo (2014). Cloud condensation nucleus activity comparison of dry- and wet-generated mineral dust aerosol: the significance of soluble material. Atmos. Chem. Phys. 14:6003-6019.

Garland, R. M., A. R. Ravishankara, E. R. Lovejoy, M. A. Tolbert and T. Baynard (2007). Parameterization for the relative humidity dependence of light extinction: Organic-ammonium sulfate aerosol. J. Geophys. Res.-Atmos. 112.

Gerber, H. E. (1979). Portable Cell for Simultaneously Measuring the Coefficients of Light-Scattering and Extinction for Ambient Aerosols. Appl. Optics 18:1009-1014.

Gong, S. L., X. Y. Zhang, T. L. Zhao, X. B. Zhang, L. A. Barrie, I. G. McKendry and C. S. Zhao (2006). A simulated climatology of Asian dust aerosol and its trans-Pacific transport. Part II: Interannual variability and climate connections. Journal of Climate 19:104-122.

Grim, R. E. (1962). Applied Clay Mineralogy, McGraw-Hill Book Company, Inc. New York, NY.

Han, Y., D. Lu, R. Z. Rao and Y. J. Wang (2009). Determination of the complex refractive indices of aerosol from aerodynamic particle size spectrometer and integrating nephelometer measurements. Appl. Optics 48:4108-4117.

Hansen, J., R. Ruedy, M. Sato and K. Lo (2010). Global Surface Temperature Change. Rev. Geophys. 48.

Hansen, J. E., A. A. Lacis, P. Lee and W. C. Wang (1980). Climatic Effect of Atmospheric Aerosols. Ann. NY Acad. Sci. 338:575-587.

Hatch, C. D., J. S. Wiese, C. C. Crane, K. J. Harris, H. G. Kloss and J. Baltrusaitis (2012). Water Adsorption on Clay Minerals As a Function of Relative Humidity: Application of BET and Freundlich Adsorption Models. Langmuir 28:1790-1803.

Haynes, W. M. (2016). Handbook of Chemistry and Physics: A Ready-Reference Book of Chemical and Physical Data. Boca Raton, FL, CRC Press.

Hecobian, A., X. Zhang, M. Zheng, N. Frank, E. S. Edgerton and R. J. Weber (2010). Water-Soluble Organic Aerosol material and the light-absorption characteristics of aqueous extracts measured over the Southeastern United States. Atmos. Chem. Phys. 10:5965-5977.

Hensen, E. J. M. and B. Smit (2002). Why clays swell. J. Phys. Chem. B 106:12664-12667.

Herbelin, J. M., J. A. McKay, M. A. Kwok, R. H. Ueunten, D. S. Urevig, D. J. Spencer and D. J. Benard (1980). Sensitive Measurement of Photon Lifetime and True Reflectances in an Optical Cavity by a Phase-Shift Method. Appl. Optics 19:144-147.

Herich, H., T. Tritscher, A. Wiacek, M. Gysel, E. Weingartner, U. Lohmann, U. Baltensperger and D. J. Cziczo (2009). Water uptake of clay and desert dust aerosol particles at sub- and supersaturated water vapor conditions. Phys. Chem. Chem. Phys. 11:7804-7809.

Hirst, E. and P. H. Kaye (1996). Experimental and theoretical light scattering profiles from spherical and nonspherical particles. J. Geophys. Res.-Atmos. 101:19231-19235.

Holben, B. N., T. F. Eck, I. Slutsker, D. Tanre, J. P. Buis, A. Setzer, E. Vermote, J. A. Reagan, Y. J. Kaufman, T. Nakajima, F. Lavenu, I. Jankowiak and A. Smirnov (1998). AERONET - A federated instrument network and data archive for aerosol characterization. Remote Sens. Environ. 66:1-16.

Hoppel, W. A. (1978). Determination of the aerosol size distribution from the mobility distribution of the charged fraction of aerosols. J. Aerosol Sci. 9:41-54.

Horvath, H. (1993). Atmospheric Light Absorption - A Review. Atmos. Environ. A-Gen 27:293-317.

Hsiao, Y.-W. and M. Hedström (2017). Swelling Pressure in Systems with Na-Montmorillonite and Neutral Surfaces: A Molecular Dynamics Study. The Journal of Physical Chemistry C 121:26414-26423.

Hsu, N. C., S. C. Tsay, M. D. King and J. R. Herman (2004). Aerosol properties over bright-reflecting source regions. IEEE T. Geosci. Remote 42:557-569.

Hudson, P. K., E. R. Gibson, M. A. Young, P. D. Kleiber and V. H. Grassian (2008). Coupled infrared extinction and size distribution measurements for several clay components of mineral dust aerosol. J. Geophys. Res.-Atmos. 113.

Humlicek, J. (2005). Handbook of Ellipsometry, William Andrew Inc. Norwich, New York.

Huneeus, N., M. Schulz, Y. Balkanski, J. Griesfeller, J. Prospero, S. Kinne, S. Bauer, O. Boucher, M. Chin, F. Dentener, T. Diehl, R. Easter, D. Fillmore, S. Ghan, P. Ginoux, A. Grini, L. Horowitz, D. Koch, M. C. Krol, W. Landing, X. Liu, N. Mahowald, R. Miller, J. J. Morcrette, G. Myhre, J. Penner, J. Perlwitz, P. Stier, T. Takemura and C. S. Zender (2011). Global dust model intercomparison in AeroCom phase I. Atmos. Chem. Phys. 11:7781-7816.

Inoue, T., S. Kuwada, D. S. Ryu and K. Osaki (1998). Effects of wavelength on strain-induced birefringence of polymers. Polym. J. 30:929-934.

IPCC, 2013: *Climate Change 2013: The Physical Science Basis. Contribution of Working Group I to the Fifth Assessment Report of the Intergovernmental Panel on Climate Change.* [T. F. Stocker, D. Qin, G. K. Plattner, M. Tignor, S. K. Allen, J. Boschung, A. Nauels, Y. Xia, V. Bex and P. M. Midgley (eds.)]. Cambridge, United Kingdom and New York, NY, USA, pp.

Jayne, J. T., D. C. Leard, X. F. Zhang, P. Davidovits, K. A. Smith, C. E. Kolb and D. R. Worsnop (2000). Development of an aerosol mass spectrometer for size and composition analysis of submicron particles. Aerosol Sci. Tech. 33:49-70.

Jenkins, F. A. and H. E. White (2001). Fundamentals of Optics, McGraw-Hill Companies, Inc. New York, New York.

Jordan, C. E., B. E. Anderson, A. J. Beyersdorf, C. A. Corr, J. E. Dibb, M. E. Greenslade, R. F. Martin, R. H. Moore, E. Scheuer, M. A. Shook, K. L. Thornhill, D. Troop, E. L. Winstead and L. D. Ziemba (2015). Spectral aerosol extinction (SpEx): a new instrument for in situ ambient aerosol extinction measurements across the UV/visible wavelength range. Atmos. Meas. Tech. 8:4755-4771.

Kebabian, P. L. and A. Freedman (2007). System and Method for Trace Species Detection Using Cavity Attenuated Phase Shift Spectroscopy with an Incoherent Light Source. U.S. Patent No. 7301639 (issued November 27, 2007).

Kebabian, P. L., W. A. Robinson and A. Freedman (2007). Optical extinction monitor using cw cavity enhanced detection. Rev. Sci. Instrum. 78.

Kelly, W. P. and P. H. McMurry (1992). Measurement of Particle Density by Inertial Classification of Differential Mobility Analyzer Generated Monodisperse Aerosols. Aerosol Sci. Tech. 17:199-212.

Kerker, M. (1969). The Scattering of Light and Other Electromagnetic Radiation, Academic Press Inc. New York, NY.

Khalizov, A. F., H. X. Xue, L. Wang, J. Zheng and R. Y. Zhang (2009). Enhanced Light Absorption and Scattering by Carbon Soot Aerosol Internally Mixed with Sulfuric Acid. J. Phys. Chem. A 113:1066-1074.

Kijne, J. W. (1969). On Interaction of Water Molecules and Montmorillonite Surfaces. Soil Sci. Soc. Am. Pro. 33:539.

Kim, H., B. Barkey and S. E. Paulson (2010). Real refractive indices of α- and β-pinene and toluene secondary organic aerosols generated from ozonolysis and photo-oxidation. J. Geophys. Res.-Atmos. 115.

Koehler, K. A., S. M. Kreidenweis, P. J. DeMott, M. D. Petters, A. J. Prenni and C. M. Carrico (2009). Hygroscopicity and cloud droplet activation of mineral dust aerosol. Geophys. Res. Lett. 36.

Kokhanovsky, A. A. and G. de Leeuw (2009). Satellite Aerosol Remote Sensing over Land, Praxis Publishing Ltd. Chichester, UK.

Koren, I., G. Dagan and O. Altaratz (2014). From aerosol-limited to invigoration of warm convective clouds. Science 344:1143-1146.

Kotchenruther, R. A., P. V. Hobbs and D. A. Hegg (1999). Humidification factors for atmospheric aerosols off the mid-Atlantic coast of the United States. J. Geophys. Res.-Atmos. 104:2239-2251.

Krejci, R., J. Strom, M. de Reus and W. Sahle (2005). Single particle analysis of the accumulation mode aerosol over the northeast Amazonian tropical rain forest, Surinam, South America. Atmos. Chem. Phys. 5:3331-3344.

Kulmala, M., M. Dal Maso, J. M. Makela, L. Pirjola, M. Vakeva, P. Aalto, P. Miikkulainen, K. Hameri and C. D. O'Dowd (2001). On the formation, growth and composition of nucleation mode particles. Tellus B. 53:479-490.

Kulp, S. and B. H. Strauss (2017). Rapid escalation of coastal flood exposure in US municipalities from sea level rise. Climatic Change 142:477-489.

Kumar, P., A. Nenes and I. N. Sokolik (2009). Importance of adsorption for CCN activity and hygroscopic properties of mineral dust aerosol. Geophys. Res. Lett. 36.

Kumar, P., I. N. Sokolik and A. Nenes (2011). Cloud condensation nuclei activity and droplet activation kinetics of wet processed regional dust samples and minerals. Atmos. Chem. Phys. 11:8661-8676.

Lack, D. A., C. D. Cappa, E. S. Cross, P. Massoli, A. T. Ahern, P. Davidovits and T. B. Onasch (2009). Absorption Enhancement of Coated Absorbing Aerosols: Validation of the Photo-Acoustic Technique for Measuring the Enhancement. Aerosol Sci. Tech. 43:1006-1012.

Lack, D. A., E. R. Lovejoy, T. Baynard, A. Pettersson and A. R. Ravishankara (2006). Aerosol absorption measurement using photoacoustic spectroscopy: Sensitivity, calibration, and uncertainty developments. Aerosol Sci. Tech. 40:697-708.

Lack, D. A., P. K. Quinn, P. Massoli, T. S. Bates, D. Coffman, D. S. Covert, B. Sierau, S. Tucker, T. Baynard, E. Lovejoy, D. M. Murphy and A. R. Ravishankara (2009). Relative humidity dependence of light absorption by mineral dust after long-range atmospheric transport from the Sahara. Geophys. Res. Lett. 36.

Lafon, S., I. N. Sokolik, J. L. Rajot, S. Caquineau and A. Gaudichet (2006). Characterization of iron oxides in mineral dust aerosols: Implications for light absorption. J. Geophys. Res.-Atmos. 111.

Lang-Yona, M., Y. Rudich, E. Segre, E. Dinar and A. Abo-Riziq (2009). Complex Refractive Indices of Aerosols Retrieved by Continuous Wave-Cavity Ring Down Aerosol Spectrometer. Anal. Chem. 81:1762-1769.

Levy, R. C., S. Mattoo, L. A. Munchak, L. A. Remer, A. M. Sayer, F. Patadia and N. C. Hsu (2013). The Collection 6 MODIS aerosol products over land and ocean. Atmos. Meas. Tech. 6:2989-3034.

Levy, R. C., L. A. Remer, R. G. Kleidman, S. Mattoo, C. Ichoku, R. Kahn and T. F. Eck (2010). Global evaluation of the Collection 5 MODIS dark-target aerosol products over land. Atmos. Chem. Phys. 10:10399-10420.

Lin, L., Z. L. Wang, Y. Y. Xu and Q. Fu (2016). Sensitivity of precipitation extremes to radiative forcing of greenhouse gases and aerosols. Geophys. Res. Lett. 43:9860-9868.

Liu, B. Y. H. and K. W. Lee (1975). Aerosol generator of high stability. Am. Ind. Hyg. Assoc. J. 36:861-865.

Liu, J. J. and Z. Q. Li (2014). Estimation of cloud condensation nuclei concentration from aerosol optical quantities: influential factors and uncertainties. Atmos. Chem. Phys. 14:471-483.

Liu, P. F., Y. Zhang and S. T. Martin (2013). Complex Refractive Indices of Thin Films of Secondary Organic Materials by Spectroscopic Ellipsometry from 220 to 1200 nm. Environ. Sci. Technol. 47:13594-13601.

Ma, X., K. Bartlett, K. Harmon and F. Yu (2013). Comparison of AOD between CALIPSO and MODIS: significant differences over major dust and biomass burning regions. Atmos. Meas. Tech. 6:2391-2401.

Ma, X. Y., J. Q. Lu, R. S. Brock, K. M. Jacobs, P. Yang and X. H. Hu (2003). Determination of complex refractive index of polystyrene microspheres from 370 to 1610 nm. Phys. Med. Biol. 48:4165-4172.

Mack, L. A., E. J. T. Levin, S. M. Kreidenweis, D. Obrist, H. Moosmuller, K. A. Lewis, W. P. Arnott, G. R. McMeeking, A. P. Sullivan, C. E. Wold, W. M. Hao, J. L. Collett and W. C. Malm (2010). Optical closure experiments for biomass smoke aerosols. Atmos. Chem. Phys. 10:9017-9026.

Massoli, P., P. L. Kebabian, T. B. Onasch, F. B. Hills and A. Freedman (2010). Aerosol Light Extinction Measurements by Cavity Attenuated Phase Shift (CAPS) Spectroscopy: Laboratory Validation and Field Deployment of a Compact Aerosol Particle Extinction Monitor. Aerosol Sci. Tech. 44:428-435.

Matheson, L. A. and J. L. Saunderson (1952). Optical and Electrical Properties of Polystyrene. Styrene: Its Polymers, Copolymers, and Derivatives. R. H. Boundy and R. F. Boyer, Reinhold Publishing Corp.**:** 517.

Matsui, H., Y. Kondo, N. Moteki, N. Takegawa, L. K. Sahu, M. Koike, Y. Zhao, H. E. Fuelberg, W. R. Sessions, G. Diskin, B. E. Anderson, D. R. Blake, A. Wisthaler, M. J. Cubison and J. L. Jimenez (2011). Accumulation-mode aerosol number concentrations in the Arctic during the ARCTAS aircraft campaign: Long-range transport of polluted and clean air from the Asian continent. J. Geophys. Res.-Atmos. 116.

May, K. R. (1973). The collison nebulizer: Description, performance and application. J. Aerosol Sci. 4:235-243.

Miles, R. E. H., S. Rudic, A. J. Orr-Ewing and J. P. Reid (2010). Influence of Uncertainties in the Diameter and Refractive Index of Calibration Polystyrene Beads on the Retrieval of Aerosol Optical Properties Using Cavity Ring Down Spectroscopy. J. Phys. Chem. A 114:7077-7084.

Miles, R. E. H., S. Rudic, A. J. Orr-Ewing and J. P. Reid (2010). Measurements of the wavelength dependent extinction of aerosols by cavity ring down spectroscopy. Phys. Chem. Chem. Phys. 12:3914-3920.

Miller, M. R., J. B. Raftis, J. P. Langrish, S. G. McLean, P. Samutrtai, S. P. Connell, S. Wilson, A. T. Vesey, P. H. B. Fokkens, A. J. F. Boere, P. Krystek, C. J. Campbell, P. W. F. Hadoke, K.

Donaldson, F. R. Cassee, D. E. Newby, R. Duffin and N. L. Mills (2017). Inhaled Nanoparticles Accumulate at Sites of Vascular Disease. ACS Nano 11:4542-4552.

Mooney, R. W., A. G. Keenan and L. A. Wood (1952). Adsorption of Water Vapor by Montmorillonite. 1. Heat of Desorption and Application of BET Theory. J. Am. Chem. Soc. 74:1367-1371.

Moosmuller, H., R. K. Chakrabarty and W. P. Arnott (2009). Aerosol light absorption and its measurement: A review. J. Quant. Spectrosc. Ra. 110:844-878.

Morang, J. L., T. Galpin and M. E. Greenslade (2018). Effective Refractive Index Values and Radiative Forcing Implications for Dry-Generated Clays as Retrieved from Cavity Ring-Down Spectroscopy. Anal. Chem. *(In Review)*.

Norrish, K. (1954). The Swelling of Montmorillonite. Discuss. Faraday Soc.:120-134.

O'Keefe, A. and D. A. G. Deacon (1988). Cavity Ring-Down Optical Spectrometer for Absorption Measurements Using Pulsed Laser Sources. Rev. Sci. Instrum. 59:2544-2551.

Pettersson, A., E. R. Lovejoy, C. A. Brock, S. S. Brown and A. R. Ravishankara (2004). Measurement of aerosol optical extinction at 532 nm with pulsed cavity ring down spectroscopy. J. Aerosol Sci. 35:995-1011.

Petzold, A., J. A. Ogren, M. Fiebig, P. Laj, S. M. Li, U. Baltensperger, T. Holzer-Popp, S. Kinne, G. Pappalardo, N. Sugimoto, C. Wehrli, A. Wiedensohler and X. Y. Zhang (2013). Recommendations for reporting "black carbon" measurements. Atmos. Chem. Phys. 13:8365-8379.

Petzold, A., T. Onasch, P. Kebabian and A. Freedman (2013). Intercomparison of a Cavity Attenuated Phase Shift-based extinction monitor (CAPS PMex) with an integrating nephelometer and a filter-based absorption monitor. Atmos. Meas. Tech. 6:1141-1151.

Prospero, J. M. (1999). Long-range transport of mineral dust in the global atmosphere: Impact of African dust on the environment of the southeastern United States. P. Natl. Acad. Sci. USA 96:3396-3403.

Prospero, J. M. and P. J. Lamb (2003). African droughts and dust transport to the Caribbean: Climate change implications. Science 302:1024-1027.

Radney, J. G., R. You, M. R. Zachariah and C. D. Zangmeister (2017). Direct In Situ Mass Specific Absorption Spectra of Biomass Burning Particles Generated from Smoldering Hard and Softwoods. Environ. Sci. Technol. 51:5622-5629.

Rogge, W. F., M. A. Mazurek, L. M. Hildemann, G. R. Cass and B. R. T. Simoneit (1993). Quantification of Urban Organic Aerosols at a Molecular Level: Identification, Abundance and Seasonal Variation. Atmos. Environ. A-Gen. 27:1309-1330.

Saleh, R., P. J. Adams, N. M. Donahue and A. L. Robinson (2016). The interplay between assumed morphology and the direct radiative effect of light-absorbing organic aerosol. Geophys. Res. Lett. 43:8735-8743.

Saltzman, E. S., G. W. Brass and D. A. Price (1983). The Mechanism of Sulfate Aerosol Formation: Chemical and Sulfur Isotopic Evidence. Geophys. Res. Lett. 10:513-516.

Sappey, A. D., E. S. Hill, T. Settersten and M. A. Linne (1998). Fixed-frequency cavity ringdown diagnostic for atmospheric particulate matter. Opt. Lett. 23:954-956.

Schepanski, K., I. Tegen and A. Macke (2009). Saharan dust transport and deposition towards the tropical northern Atlantic. Atmos. Chem. Phys. 9:1173-1189.

Schuttlefield, J. D., D. Cox and V. H. Grassian (2007). An investigation of water uptake on clays minerals using ATR-FTIR spectroscopy coupled with quartz crystal microbalance measurements. J. Geophys. Res.-Atmos. 112.

Seinfeld, J. H. and S. N. Pandis (2006). Atmospheric Chemistry and Physics, John Wiley & Sons Inc. Hoboken, NJ.

Shaw, G. E. (1983). Sun Photometry. B. Am. Meteorol. Soc. 64:4-10.

Shinozuka, Y., A. D. Clarke, A. Nenes, A. Jefferson, R. Wood, C. S. McNaughton, J. Strom, P. Tunved, J. Redemann, K. L. Thornhill, R. H. Moore, T. L. Lathem, J. J. Lin and Y. J. Yoon (2015). The relationship between cloud condensation nuclei (CCN) concentration and light extinction of dried particles: indications of underlying aerosol processes and implications for satellite-based CCN estimates. Atmos. Chem. Phys. 15:7585-7604.

Singh, S., M. N. Fiddler, D. Smith and S. Bililign (2014). Error Analysis and Uncertainty in the Determination of Aerosol Optical Properties Using Cavity Ring-Down Spectroscopy, Integrating Nephelometry, and the Extinction-Minus-Scattering Method. Aerosol Sci. Tech. 48:1345-1359.

Skoog, D. A., F. J. Holler and S. R. Crouch (2007). Principles of Instrumental Analysis, The Thomson Corporation. Belmont, CA.

Smith, J. D. and D. B. Atkinson (2001). A portable pulsed cavity ring-down transmissometer for measurement of the optical extinction of the atmospheric aerosol. Analyst 126:1216-1220.

Sorjamaa, R. and A. Laaksonen (2007). The effect of H_2O adsorption on cloud drop activation of insoluble particles: a theoretical framework. Atmos. Chem. Phys. 7:6175-6180.

Speight, J. G. (2005). Lange's Handbook of Chemistry. New York, New York, McGraw-Hill Education.

Spindler, C., A. Abo Riziq and Y. Rudich (2007). Retrieval of aerosol complex refractive index by combining cavity ring down aerosol spectrometer measurements with full size distribution information. Aerosol Sci. Tech. 41:1011-1017.

Spurny, K. R. (2005). Aerosol Measurement: Principles, Techniques, and Applications, John Wiley and Sons Inc. Hoboken, NJ.

Steimer, S. S., U. K. Krieger, Y. F. Te, D. M. Lienhard, A. J. Huisman, B. P. Luo, M. Ammann and T. Peter (2015). Electrodynamic balance measurements of thermodynamic, kinetic, and optical aerosol properties inaccessible to bulk methods. Atmos. Meas. Tech. 8:2397-2408.

Stul, M. S. and L. Vanleemput (1982). The Texture of Montmorillonites as Influenced by the Exchangeable Inorganic Cation and the Drying Method 1. External Surface-Area Related to the Stacking Units of the Aggregates. Surface Technology 16:89-100.

Stul, M. S. and L. Vanleemput (1982). The Texture of Montmorillonites as Influenced by the Exchangeable Inorganic Cation and the Drying Method 2. A Comparative Porosity Study. Surface Technology 16:101-112.

Sullivan, R. C., M. J. K. Moore, M. D. Petters, S. M. Kreidenweis, O. Qafoku, A. Laskin, G. C. Roberts and K. A. Prather (2010). Impact of Particle Generation Method on the Apparent Hygroscopicity of Insoluble Mineral Particles. Aerosol Sci. Tech. 44:830-846.

Sun, H. L., L. Biedermann and T. C. Bond (2007). Color of brown carbon: A model for ultraviolet and visible light absorption by organic carbon aerosol. Geophys. Res. Lett. 34.

Svensson, P. D. and S. Hansen (2013). Combined Salt and Temperature Impact on Montmorillonite Hydration. Clay. Clay Miner. 61:328-341.

Titos, G., A. Cazorla, P. Zieger, E. Andrews, H. Lyamani, M. J. Granados-Munoz, F. J. Olmo and L. Alados-Arboledas (2016). Effect of hygroscopic growth on the aerosol light-scattering coefficient: A review of measurements, techniques and error sources. Atmos. Environ. 141:494-507.

Tong, D. Q., J. X. L. Wang, T. E. Gill, H. Lei and B. Y. Wang (2017). Intensified dust storm activity and Valley fever infection in the southwestern United States. Geophys. Res. Lett. 44:4304-4312.

Toon, O. B., J. B. Pollack and B. N. Khare (1976). The optical constants of several atmospheric aerosol species: Ammonium sulfate, aluminum oxide, and sodium chloride. J. Geophys. Res. 81:5733-5748.

Twomey, S. A., M. Piepgrass and T. L. Wolfe (1984). An Assessment of the Impact of Poluttion on Global Cloud Albedo. Tellus B. 36:356-366.

Uno, I., K. Eguchi, K. Yumimoto, T. Takemura, A. Shimizu, M. Uematsu, Z. Y. Liu, Z. F. Wang, Y. Hara and N. Sugimoto (2009). Asian dust transported one full circuit around the globe. Nature Geoscience 2:557-560.

van de Hulst, H. C. (1981). Light Scattering by Small Particles, Dover Publications Inc. Mineola, NY.

Veghte, D. P., J. E. Moore, L. Jensen and M. A. Freedman (2015). Influence of shape on the optical properties of hematite aerosol. J. Geophys. Res.-Atmos. 120:7025-7039.

Virtanen, A., J. Joutsensaari, T. Koop, J. Kannosto, P. Yli-Pirila, J. Leskinen, J. M. Makela, J. K. Holopainen, U. Poschl, M. Kulmala, D. R. Worsnop and A. Laaksonen (2010). An amorphous solid state of biogenic secondary organic aerosol particles. Nature 467:824-827.

Waggoner, A. P., R. E. Weiss, N. C. Ahlquist, D. S. Covert, S. Will and R. J. Charlson (1981). Optical Characteristics of Atmospheric Aerosols. Atmos. Environ. 15:1891-1909.

Washenfelder, R. A., J. M. Flores, C. A. Brock, S. S. Brown and Y. Rudich (2013). Broadband measurements of aerosol extinction in the ultraviolet spectral region. Atmos. Meas. Tech. 6:861-877.

Wheeler, M. D., S. M. Newman, A. J. Orr-Ewing and M. N. R. Ashfold (1998). Cavity ring-down spectroscopy. J. Chem. Soc. Faraday T. 94:337-351.

Wiegand, J. R., L. D. Mathews and G. D. Smith (2014). A UV-Vis Photoacoustic Spectrophotometer. Anal. Chem. 86:6049-6056.

Xu, W. Z., C. T. Johnston, P. Parker and S. F. Agnew (2000). Infrared study of water sorption on Na-, Li-, Ca-, and Mg-exchanged (SWy-1 and SAz-1) montmorillonite. Clay. Clay Miner. 48:120-131.

Yu, H. B., L. A. Remer, M. Chin, H. S. Bian, Q. Tan, T. L. Yuan and Y. Zhang (2012). Aerosols from Overseas Rival Domestic Emissions over North America. Science 337:566-569.

Zarzana, K. J., C. D. Cappa and M. A. Tolbert (2014). Sensitivity of Aerosol Refractive Index Retrievals Using Optical Spectroscopy. Aerosol Sci. Tech. 48:1133-1144.

Zender, C. S., H. S. Bian and D. Newman (2003). Mineral Dust Entrainment and Deposition (DEAD) model: Description and 1990s dust climatology. J. Geophys. Res.-Atmos. 108.

Zhang, J. L., J. S. Reid, R. Alfaro-Contreras and P. Xian (2017). Has China been exporting less particulate air pollution over the past decade? Geophys. Res. Lett. 44:2941-2948.

Zhang, X. Y., Y. Q. Wang, T. Niu, X. C. Zhang, S. L. Gong, Y. M. Zhang and J. Y. Sun (2012). Atmospheric aerosol compositions in China: spatial/temporal variability, chemical signature, regional haze distribution and comparisons with global aerosols. Atmos. Chem. Phys. 12:779-799.

Zhao, W., X. Xu, M. Dong, W. Chen, X. Gu, C. Hu, Y. Huang, X. Gao, W. Huang and W. Zhang (2014). Development of a cavity-enhanced aerosol albedometer. Atmos. Meas. Tech. 7:2551-2566.